TAMPERE UNIVERSITY OF TECHNOLOGY

JUAN QUINTANA

RADIATED RF PERFORMANCE MEASUREMENTS FOR 4G MOBILE TERMINALS

Master of Science thesis

Examiners: Professor Mikko Valkama and Dr.(Tech.) Jari Kangas
Examiners and topic approved by the Faculty Council of the Faculty of Computing and Electrical Engineering on 5 March 2014

ABSTRACT

TAMPERE UNIVERSITY OF TECHNOLOGY
Master's Degree Program in Electrical Engineering
QUINTANA, JUAN: Radiated RF Performance Measurements for 4G Mobile Terminals
Master of Science Thesis, 72 pages
April 2014
Major: RF Electronics
Examiners: Professor Mikko Valkama and Dr.(Tech.) Jari Kangas
Keywords: Radio Frequency (RF), radiated measurements

Radio Frequency (RF) measurements are a fundamental stage in the design, testing and optimization of radio systems. Different parameters are evaluated in order to ensure fulfillment of given design specifications. In addition to these, it has become mandatory for every manufacturer of RF equipment to comply with a set of specifications devised by regulatory entities in order to guarantee that different RF products will work together in an environment where deleterious interference among them is minimized.

Mobile phones have emerged as perhaps the most emblematic and mass-produced RF devices to date. Nokia Corporation has a portfolio of smart devices known as Lumia phones. This thesis is part of a project carried out in this company in order to evaluate the performance of different RF parameters on such phones. Manufactures of RF devices have recently begun to evaluate RF parameters in a radiated manner by using a fairly straightforward setup that includes a radio communication tester, an RF shield box and an antenna coupler. This thesis provides a study on radiated RF measurements performed on 4G mobile terminals in the setup described above. Even though it may be presumed a similar study may already exist from other manufacturers, such information is rarely forthcoming due to confidentiality issues. Nokia Corporation has allowed the author to conduct such study in a way where the most fundamental principles of the measurement setup in question are highlighted and the RF performance of 4G phones is evaluated in that setup. The results presented herein include those obtained from measurements made in both the reactive and radiating near-field regions. I will establish the legitimacy of the results obtained in both regions, provided the phone is placed at an appropriate position, termed sweet spot. I propound three criteria to find that sweet spot. In order to verify the validity of my measurements, a process capability analysis will be conducted to demonstrate the compliance of the results to given specifications. An outline of the procedure to further verify the results is also presented at the end of the thesis. Finally, I will propose further investigations that may be derived from this thesis, from computational studies to a deeper analysis of uncertainties.

PREFACE

This Master of Science thesis was part of a project carried out at Nokia Corporation in Tampere, Finland.

I wish to dedicate it to my God. My creator, my redeemer, my sanctifier. Boundless source of my happiness, my joy, my hope, my longings. Indeed, I cannot but concur: 'My heart is restless until the instant it will begin to rest in Thee.'

To my family, for their unfaltering encouragement: my dear parents Guillermo and María Rita, my siblings Manuel, Gilma, Esperanza, Robert, Yolima, and Milena, and to my nephews and nieces.

To the Finnish people. They have been really generous to a fault. I wish to thank my thesis supervisors in Nokia, Samuli Pietilä and Petri Ranni, for their constant support and invaluable feedback throughout my thesis. Equally inestimable was the assistance provided by my colleagues: Jarno Luukkonen, Teemu-Juhani Rajala, Anttoni Rautio, Pekka Halme and Aimo Arkko. I also wish to extend my deep appreciation to my examiners at Tampere University of Technology: Dr.(Tech.) Jari Kangas and Professor Mikko Valkama. Their insightful revisions on my thesis manuscripts were undoubtedly crucial to the completion of a text scientifically palatable and coherent.

This thesis is the culmination of a journey I set out to broaden my knowledge, and treasured knowledge have I acquired. I am greatly indebted for that to many of my instructors in the RF electronics program: Dr.(Tech.) Jari Kangas, Dr.(Tech.) Olli-Pekka Lundén, Dr.(Tech.) Jouko Heikkinen, Dr.(Tech.) Tiiti Kellomäki, Dr.(Tech.) Riku Mäkinen, to name a few. This is but a small token of appreciation to your arduous and outstanding dedication. My learning experience would have been wanting, had it not been for the splendid opportunity given to advance my career at Nokia Corporation. I want to thank my managers and colleagues for contributing to this achievement.

Finally, I wish to express my sincere gratefulness to my parish priests, Fr. Zenon Strykowski and Fr. Stanisław Zawiłowicz for their spiritual guidance, and to all my friends for their support.

Tampere, April 15 2014.

Juan Quintana

CONTENTS

TERMS AND ABBREVIATIONS

SYMBOLS

$\mathbf{A}$	magnetic vector potential [Wb/m]
β	phase constant [rad/m]
dB	decibel
ϵ	permittivity [F/m]
Γ	voltage reflection coefficient
$\jmath$	electric current density [A/m^2]
λ	wavelength [m]
k	wave number [1/m]
μ	permeability [H/m]
μ	true arithmetic mean
μ_C	combined standard uncertainty
η	wave impedance [Ω]
ρ	charge density [C/m^3]
σ	conductivity [S/m]
σ	standard deviation
ϕ	azimuth angle [deg]
Φ	(electric) scalar potential [V]
ψ	phase shift [deg]
θ	elevation angle [deg]
v_p	velocity of propagation [m/s]
ω	angular frequency [rad/s]
X	continuous random variable
Z	impedance [Ω]

ABBREVIATIONS

ACLR	Adjacent Carrier Leakage Ratio
BER	Bit Error Rate
Cp	Process Potential
Cpk	Process capability (NB: Minitab®16 computes and displays this parameter as Ppk)
DL	Downlink
DUT	Device Under Test
EM	Electromagnetic
E-UTRA	Evolved Universal Terrestrial Radio Access
EVM	Error Vector Magnitude

FDD	Frequency Division Duplex
GPS	Global Positioning System
GSM	Global System for Mobile Communications
HPBW	Half Power Beamwidth
LCL	Lower Control Limit
LHCP	Left Hand Circularly Polarized
LSL	Lower Specification Limit
LTE	Long Term Evolution
MR	Moving Range
MS	Mobile Station
OTA	Over the Air
Pp	Process performance
Ppk	Overall process performance (This corresponds to Cpk parameter in Minitab®16)
QPSK	Quadrature Phase Shift Keying
RF	Radio Frequency
RHCP	Right Hand Circularly Polarized
RMS	Root Mean Square
RX	Receiving
TDD	Time Division Duplex
TEM	Transverse Electromagnetic
TX	Transmitting
UCL	Upper Control Limit
UE	User Equipment
UMTS	Universal Mobile Telecommunication System
UP	Uplink
USL	Upper Specification Limit
VNA	Vector Network Analyzer
VSWR	Voltage Standing Wave Ratio
WCDMA	Wideband Code Division Multiple Access
WLAN	Wireless Local Area Network
2G	Second Generation
3G	Third Generation
3GPP	3rd Generation Partnership Project
4G	Fourth Generation

1. INTRODUCTION

A fundamental component of a wireless cellular communication system is the mobile handset, also known as mobile station (MS) or user equipment (UE). Early second generation (2G) cellular technologies boasted handsets with robust voice and messaging capabilities. As it turned out, however, the continuous advancements in integrated circuit (IC) design and signal processing techniques along with the advent of the Internet proved to be a watershed in the subsequent development of more sophisticated technologies known as third generation (3G) and at present, fourth generation (4G). Such technologies have been able to respond satisfactorily to the ever increasing demand from users of not only voice and messaging services but more importantly, of data services requiring large amounts of bandwidth and acceptable error rates and delays to ensure an optimum quality of service. This has brought new challenges to the design of networks and handsets and yet, it has given rise to a new generation of state-of-the-art devices known as smart phones. A great deal of the brunt these challenges pose has been borne by the handsets on their radio frequency (RF) performance. A critical stage in the design of smart phones, RF performance quantifies the level of functionality of every handset unit according to specifications set by network operators and regulatory entities, and has an impact on the performance of the cellular network as a whole, in terms of the coverage and capacity it is meant to offer.

RF performance parameters have been typically evaluated by means of conducted RF measurements. In this type of setting, a coaxial cable is connected from a radio communication tester directly to the antenna port connection from the phone under test and the RF parameters are evaluated. In other words, conducted measurements omit the antenna structure and sense the electromagnetic fields directly from the printed circuit board (PCB). In this way, no radiated fields are tested but rather those (arriving at the connection port) that are confined by the transmission lines on the RF stage of the phone. Conducted RF measurements are crucial during the design process where prototypes are fabricated, tested, optimized, and re-tested until a final product capable of meeting the design specifications is made. The approach of conducted RF measurements implies that the performance of the phone is evaluated without considering the antenna performance itself. This indeed is problematic since the antenna represents a fundamental component to the functioning of the phone.

However, final products with all the mechanics (antennas, covers) incorporated are tested in over-the-air (OTA) environments to account for the performance of the whole phone handset. These measurements are made in anechoic or reverberation chambers where a free-space environment is emulated. These chambers, however, are very expensive and are mostly used for stand-alone antenna measurements made by antenna designers. Alternatively, radiated RF measurements can be performed using different measurement setups. For instance, [1] suggests four methods to measure the radiated power from mobile phones. They range from a near-field-far-field radiation pattern transformation, to using a microwave near-field scanner to measure the radiation pattern and radiated power from the phone.

This thesis will present an additional method that has gained popularity among manufacturers of mobile phones. This method uses a simple measurement setup consisting mainly of a radio communication tester, an RF shield box, and an antenna coupler. My main intent is to evaluate the most relevant RF parameters on 4G phones using the above setup. Results will be subject to a statistical process capability analysis to ensure conformance to specifications. This will allow me to verify the reliability and accuracy of the measurements and will implicitly validate the reliability and sturdiness of the measurement setup. In addition, I will indicate a further step undertaken to corroborate my results. The measurement results that I present herein have been made in the two sub-regions that comprise the near-field region, namely, the reactive and the radiating regions. A comparative analysis of the two settings will be included and the validity of the corresponding results will be explored.

This thesis is structured as follows: a theoretical background chapter introduces the reader into the most relevant concepts needed to understand the nature of the measurements made, and to gain insight into the measurement system and the necessary tools used to analyze the results data. A chapter devoted to an analysis of the measurement system delves into the description of the measurement setup, both at the component level and as a whole. It also introduces the concept of sweet spot. A subsequent chapter presents the test settings and specifications to be met, as well as the process capability output calculated from the measurement results. Finally, some conclusions culminate this thesis.

2. THEORETICAL BACKGROUND

This chapter is intended to provide a theoretical foundation needed for an adequate understanding of the measurements carried out in this project and the subsequent analysis of the results. Evidently, a thorough study of all the theoretical concepts involved would demand a time and space exceeding the scope of this thesis and in any case, it would result in a redundant treatise since the reader is given all necessary references for further reading. This chapter begins with an introduction of the fundamentals of electromagnetics followed by an study of antennas as they constitute a key component of the mobile handsets and the coupler used in the measurement setup. Finally, a section describes the basics of statistics and process capability assessment used to analyze the measurement results in a subsequent chapter.

2.1 Fundamentals of Electromagnetics

Electromagnetic phenomena must be analyzed in the two ways they are manifested: that of statics and that of time-varying fields. Electrostatics and magnetostatics refer to stationary fields and as such they are of no interest in the present work. They may be said to be a special case of electromagnetic fields. A more general description of electromagnetic phenomena must include an analysis of time-varying fields as they give rise to electromagnetic waves. Electromagnetic waves can be carried via conducted media, such as a coaxial cable or a waveguide, or can be transmitted/received over the free space via radio links.

Time-varying fields imply waves oscillating at a given frequency. Wireless communication systems typically utilize high frequency carrier signals. The reasons that justify the use of high frequencies in communication systems are manifold [2, p.2] and encompass the attainment of higher antenna gains and bandwidths, as well as the ability to withstand ionospheric bending effects on line-of-sight satellite communications. At present, cellular communication systems have been assigned frequency bands ranging from the 700 MHz to the 2500 MHz. This range falls in the category of radio frequency (RF). Some authors, for example [2, p. 2], have suggested the inclusion of this range into a far more encompassing classification of microwave frequencies, which include millimeter waves commonly used in radar systems. In our case, we will keep the more common convention of RF for our frequencies of interest. Regardless of the frequency used, any time-varying field is described by a

set of invaluable tools known as Maxwell's equations. The description that follows is confined to the application of Maxwell's equations to time-varying fields alone. Likewise, the analysis is circumscribed to homogeneous, linear isotropic propagation media. A material is said to be homogeneous if its characteristics do not depend on position and is isotropic if its behavior remains unaltered regardless of the direction of any of the field vectors [3].

2.1.1 Maxwell's equations

A comprehensive study of how Maxwell's equations are obtained can be found in [3] and [4] and in fact, most of the following discussion is derived from there. Maxwell's equations can be written in differential, integral or phasor form for convenience. Before presenting the equations per se, let us first introduce the quantities that make up the body of the equations. Table 2.1 summarizes these main quantities.

Table 2.1: Major quantities of Maxwell's equations

Symbol	**Quantity**	**Units**
$\vec{D}$	electric flux density	C/m^2
$\vec{B}$	magnetic flux density	Wb/m^2
$\vec{E}$	electric field intensity	V/m
$\vec{H}$	magnetic field intensity	A/m
$\vec{j}$	electric current density	A/m^2
ρ	charge density	C/m^3

A set of constitutive relations link the above field quantities as follows:

$$\begin{aligned} \vec{D} &= \epsilon\vec{E} = \epsilon_r\epsilon_0\vec{E}, \\ \vec{B} &= \mu\vec{H} = \mu_r\mu_0\vec{H}, \\ \vec{j} &= \sigma\vec{E}, \end{aligned}$$

where σ represents the conductivity of a material in Siemens per meter $[S/m]$ and ϵ is known as the *absolute permittivity* or *permittivity* of the propagation medium and it comprises the permittivity of free space, $\epsilon_0 \cong (1/36\pi) \times 10^{-9}[F/m]$, and the dimensionless constant ϵ_r representing the *relative permittivity* or *dielectric constant*, which characterizes the dielectric properties of a given material. On the other hand, the *permeability* μ can be split into the permeability of free space, $\mu_0 = 4\pi \times 10^{-7}[H/m]$, and the relative permeability μ_r which is another constant that depends on the material. It should be noted that ϵ_r and μ_r are taken to be real scalar quantities as it applies for linear isotropic, homogeneous media. In addition to the above constitutive relations, an extremely important force law relating the electric

and magnetic fields and known as the Lorentz force is given as

$$\vec{F} = q(\vec{E} + \vec{v} \times \vec{B})[N],$$

and states that a force is created for a charge q that is moving with a velocity $\vec{v}$ through an electric field $\vec{E}$ and magnetic flux density $\vec{B}$.

Maxwell's equations as we know them today are commonly expressed in their differential form as follows:

$$\nabla \cdot \vec{D} = \rho, \tag{2.1}$$

$$\nabla \cdot \vec{B} = 0, \tag{2.2}$$

$$\nabla \times \vec{E} = -\frac{\partial \vec{B}}{\partial t}, \tag{2.3}$$

$$\nabla \times \vec{H} = \vec{j} + \frac{\partial \vec{D}}{\partial t}. \tag{2.4}$$

In their differential form, Maxwell's equations are written as real functions of Cartesian coordinates (x, y, z) and time coordinate t. Equation (2.1) is widely known as Gauss's law for electricity and it describes how an electric flux per unit volume amounts to the total charge density enclosed by such volume. Interestingly enough, equation (2.2) states that the divergence of the magnetic field is zero everywhere. In other words, the magnetic flux lines always close upon themselves which stems from the fact that magnetic flow sources do not exist. Equation (2.3) is known as Faraday's law and states that the rate of change of the magnetic flux generates or induces an electric field. In its original postulate, Faraday's law is written in integral form as the rate of change of the integral of the magnetic flux over a surface, which gives rise or induces an electromotive force. In turn, the electromotive force equals the line integral of the electric field about a closed path. Equation (2.3) is just the differential form of Faraday's law and can be readily obtained by applying Stoke's theorem to the integral equation just described. Finally, equation (2.4) contains the statics term of electric current density $\vec{j}$ ($\nabla \times \vec{H} = \vec{j}$ constitutes Ampère's law) and introduces one of the main contributions of Maxwell to the theory of electromagnetism and that is the concept of displacement current density, denoted by the term $\frac{\partial \vec{D}}{\partial t}$. Maxwell realized that if the principle of charge conservation was not to be violated in the time varying case, a displacement current density term should be included. It is the latter along with the Faraday's law postulate of the generation of electric fields from changing magnetic fields that essentially account for the phenomena of wave propagation, resonance, and radiation [3].

As mentioned, Maxwell's equations can also be written in integral and phasor form. The integral form becomes very convenient when the equations need to pro-

vide information of overall regions of space, for example objects with specific shapes and boundaries. The phasor counterpart becomes relevant when the variation of the electromagnetic fields is dictated by steady-state AC fields varying sinusoidally in time. This is also known as the time-harmonic case and it is perhaps the most common situation found in engineering applications. Notice that the field quantities in the phasor form differ from those in the differential and integral counterparts in that they represent the complex multipliers of the term $e^{j\omega t}$ and hence are termed *phasors*. Typically, phasor quantities are written in boldface scripts to avoid confusion. The integral and phasor forms of Maxwell's equations are summarized below.

Integral form

$$\begin{aligned}
\oint_S \vec{D} \cdot d\vec{S} &= \int_V \rho dV, \\
\oint_S \vec{B} \cdot d\vec{S} &= 0, \\
\oint \vec{E} \cdot \vec{dl} &= -\frac{\partial}{\partial t} \int_S \vec{B} \cdot d\vec{S}, \\
\oint \vec{H} \cdot \vec{dl} &= \int_S \vec{\jmath} \cdot d\vec{S} + \frac{\partial}{\partial t} \int_S \vec{D} \cdot d\vec{S}.
\end{aligned}$$

Phasor form

$$\nabla \cdot \boldsymbol{D} = \rho, \tag{2.5}$$

$$\nabla \cdot \boldsymbol{B} = 0, \tag{2.6}$$

$$\nabla \times \boldsymbol{E} = -j\omega \boldsymbol{B}, \tag{2.7}$$

$$\nabla \times \boldsymbol{H} = \boldsymbol{\jmath} + j\omega \boldsymbol{D}. \tag{2.8}$$

Boundary conditions

A set of boundary conditions has to be imposed for the solution of Maxwell's equations when calculating the electromagnetic fields. These boundary conditions hold when the plane wave travels an interface between two or more media. Each medium will be characterized by the material's properties, that is μ, ϵ and σ. The main boundary conditions are summarized below in their scalar form[5, p. 312]

$$E_{t1} = E_{t2}, \tag{2.9}$$

$$H_{t1} - H_{t2} = J, \tag{2.10}$$

$$B_{n1} = B_{n2}, \tag{2.11}$$

$$D_{n1} - D_{n2} = \rho, \tag{2.12}$$

$$J_{n1} = J_{n2}, \tag{2.13}$$

$$\frac{J_{n1}}{\sigma_1} = \frac{J_{n2}}{\sigma_2}, \tag{2.14}$$

where the subscripts $t1$ and $t2$ represent the components of the fields tangential to the boundary in media 1 and 2, respectively, while the subscripts $n1$ and $n2$ refer to those components that are normal to the boundary. Equation (2.9) tells that the tangential components of the electric fields at the boundary are the same, whereas those of the magnetic fields are discontinuous by an amount equivalent to the electric current density as stated in equation (2.10).

Equation (2.11) states that the normal components of the magnetic flux densities at the interface are equal and yet, equation (2.12) states that the normal components of the electric flux densities are discontinuous by a value equal to the charge density.

The normal components of the electric current densities are equal at the interface as equation (2.13) asserts. and equation (2.14) states that the ratio of the tangential components of the electric currents densities at the interface equals the ratio of the conductivities of their respective media.

When the above boundary conditions are specified along with the initial conditions of the fields at time zero, the solutions to the electromagnetic fields can be said to be unique [3, p. 258]. The foregoing analysis would seem at first to be more relevant for regions with closed boundaries clearly defined by conductors and dielectric materials, such as in the case of wave-guiding structures. However, a unique solution condition should also be satisfied when the fields propagate in open regions extending to infinity. This is fulfilled by enforcing certain *radiation conditions* which ensure that the principle of energy conservation in not violated. Thus, if r is the distance separating the radiation source from the point in an open region where the fields are assessed, the radiation conditions require that the results from the products $r\vec{E}$ and $r\vec{H}$ remain finite as r tends to infinity. These conditions hold when the electromagnetic fields are generated from real charge and current sources which are enclosed in a finite region [3, p. 259]. An analysis of the calculation of radiated fields will be presented in the section dealing with radiation.

2.1.2 Plane Waves

The previous sections described Maxwell's equations in their different forms and underscored the significance of the equations when we set out to analyze electromagnetic fields. Let us explore electromagnetic waves in more detail by analyzing the concept of a plane wave. For that, let us assume a region in space containing no sources and which is also linear, isotropic, and homogeneous. Therefore, Maxwell's curl equations in phasor form are reduced to

$$\begin{aligned} \nabla \times \boldsymbol{E} &= -j\omega\mu\boldsymbol{H}, \\ \nabla \times \boldsymbol{H} &= -j\omega\epsilon\boldsymbol{E}. \end{aligned}$$

After some manipulation, it can be demonstrated [2, p. 15] that these equations yield

$$\nabla^2\boldsymbol{E} + \omega^2\mu\epsilon\boldsymbol{E} = 0, \tag{2.15}$$

$$\nabla^2\boldsymbol{H} + \omega^2\mu\epsilon\boldsymbol{H} = 0, \tag{2.16}$$

where equation (2.15) is known as Helmholtz equation or wave equation for $\vec{E}$, and (2.16) is the wave equation for $\vec{H}$. The term $k = \omega\sqrt{\mu\epsilon}$ $[m^{-1}]$ is defined as the wavenumber, or propagation constant of the medium and is also commonly denoted by β. A basic plane wave solution to equation (2.15) can be obtained by considering a wave with a uniform electric field on planes that are perpendicular to z, so that $\frac{\partial^2 E_x}{\partial x^2} = \frac{\partial^2 E_x}{\partial y^2} = 0$. The resultant uniform plane wave equation is

$$\frac{\partial^2 E_x}{\partial z^2} + k^2 E_x = 0. \tag{2.17}$$

The solutions to this homogeneous equation will be of the form

$$E_x(z) = E^+ e^{-jkz} + E^- e^{jkz}, \tag{2.18}$$

where E^+ and E^- are arbitrary constants determined by boundary conditions. The solution is in phasor form. The instantaneous wave expression[1] for a cosine reference is

$$\vec{E}(z,t) = [E^+\cos(\omega t - kz) + E^-\cos(\omega t + kz)]\vec{a_x}. \tag{2.19}$$

The first term on the right side of equation (2.19) represents a travelling wave propagating in the positive z direction, and the second term is a wave traveling in the negative z direction.The velocity of propagation or *phase velocity* of the wave is

[1] A solution to equation (2.17) is often obtained by direct substitution of any function in the variable $t - z/v_p$, where v_p is the propagation velocity [3, p. 25].

given by $v_p = \frac{1}{\sqrt{\mu\epsilon}}$ $[m/s]$ and the wavelength is $\lambda = \frac{v_p}{f}$ $[m]$, where f is the frequency in $[Hz]$. Another important parameter denoted as the *intrinsic impedance* of the medium is given as $\eta = \sqrt{\frac{\mu}{\epsilon}}$ $[\Omega]$. In vacuum, $v_p = \frac{1}{\sqrt{\mu_0\epsilon_0}} = 2,998 \times 10^8$ m/s and $\eta = \sqrt{\frac{\mu_0}{\epsilon_0}} = 120\pi = 377\ \Omega$. Furthermore, the electric $\vec{E}$ and magnetic $\vec{H}$ fields are perpendicular to each other [3, p. 324]. At an instantaneous moment, the value of $\vec{E}$ is η times that of the $\vec{H}$ field and they will be orthogonal to the direction of propagation. Transverse electromagnetic waves are characterized by these properties. Thus, intrinsic impedance relates equation (2.19) to its accompanying magnetic field by

$$\vec{H} = \frac{\vec{a_y}}{\eta}[E^+ \cos(\omega t - kz) - E^- \cos(\omega t + kz)].$$

Polarization of plane waves

The polarization of a plane wave is defined as the pattern that is traced out by the instantaneous electric field vector with time at a fixed location [6, p. 62]. The simplest case is found when the the electric field vector oscillates along a line so that if an observer, located orthogonally and oppositely to the propagating wave, were to fix his attention at a given point on the wave component traced out by the electric field vector, he would see a line whose magnitude would oscillate between a maximum and a minimum. In this case the plane wave is said to be *linearly* polarized. Another case is seen when two uniform plane waves of the same frequency, but different phases, magnitudes, and orientations of the field vectors are superposed. In this case the resultant pattern is an ellipse and thus the wave is said to be *elliptically* polarized. This is more readily seen by breaking the wave into its two components, that is, the electric field components in the x and y axes. Let us assume that the y component leads the x component by a phase ψ. Thus, the field expressions are given as

$$\begin{aligned} E_x &= E_1 \cos(\omega t - kz), \\ E_y &= E_2 \cos(\omega t - kz + \psi). \end{aligned}$$

At $z = 0$, these equations reduce to $E_x = E_1 \cos \omega t$ and $E_y = E_2 \cos(\omega t + \psi)$ which correspond to the parametric equations for an ellipse.

If the two waves combined have equal x and y components, and the phase difference is 90°, the ellipse becomes a circle, and the wave is said to be *circularly* polarized. In this case $\psi = \pm\pi/2$, $E_1 = E_2 = E$ and thus by adding the squared x and y components we arrive at $E^2 = E_x^2 + E_y^2$, which is nothing less than the equation of a circle. An instantaneous angle α between the electric field vector and the x axis at $z = 0$ is defined as

$$\alpha = \tan^{-1}\left(\frac{E_y}{E_x}\right) = \tan^{-1}\left(\frac{\mp E \sin \omega t}{E \cos \omega t}\right) = \mp \omega t,$$

which shows that the electric field vector rotates at a uniform rate $\omega = 2\pi f$. Our observer will see a left-hand circularly polarized wave traveling towards him if the electric field vector rotates in a clockwise sense, and that occurs when $\psi = +\pi/2$. Conversely, $\psi = -\pi/2$ gives rise to a right-hand circularly polarized wave as seen by the same observer.

Poynting's theorem and energy considerations

Electromagnetic waves have the inherent property of carrying power. The amount of energy being transferred depends on the magnitudes, distribution, and phases of the electric and magnetic fields of the wave [3]. A fundamental law of physics, that of the conservation of energy, becomes evident in electromagnetic systems when a power balance is performed. *Poynting's theorem* formulates this power balance as [2]

$$-\oint_S (\vec{E} \times \vec{H}) \cdot d\vec{S} = \frac{\partial}{\partial t} \int_V \left(\frac{1}{2}\epsilon \vec{E}^2 + \frac{1}{2}\mu \vec{H}^2 \right) dV + \int_V \sigma \vec{E}^2 dV. \tag{2.20}$$

The term on the left side of equation (2.20) represents the power that traverses the surface S enclosing the volume V. The negative sign indicates that the power is flowing into the volume. A positive sign would have meant a power flow out of the volume. The first and second terms on the right side of equation (2.20) are the time-rate of change of the stored energy in the electric and magnetic fields, respectively. The positive sign in both terms means that some external source supplies the energy to be stored in the electric and magnetic fields. Were it negative, the sign would indicate that the energy is deducted from the fields. The last term on the right side of the equation represents the power supplied to the charged particles by the electric field and is known as the ohmic loss term because it represents the energy dissipated in heat. The vector product on the left side of the equation is called the *Poynting vector* $\vec{S}$, that is

$$\vec{S} = \vec{E} \times \vec{H} \ [W/m^2],$$

and it yields the instantaneous power flow per unit area. A very important concept can be further developed when we consider the case of time-harmonic electromagnetic waves. Equation (2.19) gave us the instantaneous wave expression for a cosine referenced electric field. For simplicity, let us consider only the waves propagating in the positive z direction so that the instantaneous expressions for the waves are

$$\vec{E}(z,t) = E^+ \cos(\omega t - kz), \quad \vec{H}(z,t) = \frac{1}{\eta} E^+ \cos(\omega t - kz).$$

[2] to see how the theorem is derived from the curl Maxwell's equations, check [4, p. 298].

The Poynting vector in this case will be given by

$$\vec{S}(z,t) = \vec{E}(z,t) \times \vec{H}(z,t) = \frac{E^{+^2}}{\eta} \cos^2(\omega t - kz).$$

As interesting as the instantaneous power is, a more significant quantity can be deduced if the above Poynting vector is integrated over a time period of the wave, $T = \frac{2\pi}{\omega}$. So the *average power density* carried by an uniform plane wave traveling in the positive z direction (again, for the lossless case) is given by

$$\vec{S}_{av}(z) = \frac{1}{T} \int_0^T S(z,t)dt = \frac{E^{+^2}}{2\eta} \; [W/m^2].$$

In a more general case accounting for the wave traveling in any direction, the average power density expression is written as

$$\vec{S}_{av} = \frac{1}{2} Re(\mathbf{E} \times \mathbf{H}^*) \tag{2.21}$$

where * denotes complex conjugation. If losses are to be taken into account in the above analysis, an attenuation constant α and a phase angle of the intrinsic impedance θ_η should be included as shown in [4, p. 301].

2.1.3 Radiation

The previous sections have described how Maxwell's equations are used to analyze and characterize electromagnetic fields. The concept of plane waves was also introduced as an important example of electromagnetic phenomena. A paramount requirement for radiation to occur is that the conductor generating the fields that will propagate in the open regions must be excited by a time-varying voltage or current source. This allows the acceleration (or deceleration) of electrons in the conductor, which accounts for radiation to happen [7, p. 1]. An analysis of the radiated waves must necessarily start with a solution of Maxwell's equations. That will solve for the electromagnetic fields that are radiated due to a time-varying current. We have seen in equation (2.4) that the sources of a magnetic field are the displacement current and the electric current density. The latter is also referred to as the *current distribution* in most antenna books and we will show next how, following a discussion presented in [6], a solution to the electromagnetic fields can be readily obtained if we know the current distribution. A solution to the fields is greatly facilitated by the introduction of a pair of potential functions, a scalar

potential Φ and a magnetic vector potential $\boldsymbol{A}$[3].

The divergence of a magnetic field is zero not only in the static case but also in general. Therefore, the vector field $\boldsymbol{B}$ has only circulation and thus is called a solenoidal field. As such, it can be represented by the curl of some other vector function, say $\boldsymbol{A}$, and hence we obtain

$$\begin{aligned} \boldsymbol{B} &= \nabla \times \boldsymbol{A}, \quad or \\ \boldsymbol{H} &= \frac{1}{\mu} \nabla \times \boldsymbol{A}. \end{aligned} \tag{2.22}$$

Equation (2.7) can be rewritten then as

$$\nabla \times (\boldsymbol{E} + j\omega \boldsymbol{A}) = 0. \tag{2.23}$$

This equation implies that the curl of the vector quantity in parenthesis is zero. This condition allows us to derive the vector as a gradient, for instance Φ. Thus we obtain

$$\boldsymbol{E} + j\omega \boldsymbol{A} = -\nabla \Phi \quad or \quad \boldsymbol{E} = -j\omega \boldsymbol{A} - \nabla \Phi. \tag{2.24}$$

The electric field $\boldsymbol{E}$ is now expressed in terms of a scalar and a vector potential. By substituting (2.24) into equation (2.5) we obtain

$$-\nabla^2 \Phi - j\omega \nabla \cdot \boldsymbol{A} = \frac{\rho}{\epsilon}. \tag{2.25}$$

Next, (2.22) and (2.24) can be substituted into equation (2.8) to obtain

$$\nabla \times \nabla \times \boldsymbol{A} = \mu \boldsymbol{\jmath} + \mu\epsilon[-j\omega \nabla \Phi + \omega^2 \boldsymbol{A}].$$

A vector identity, $\nabla \times \nabla \times \boldsymbol{A} = \nabla(\nabla \cdot \boldsymbol{A}) - \nabla^2 \boldsymbol{A}$, can be used to transform the latter into

$$\nabla(\nabla \cdot \boldsymbol{A}) - \nabla^2 \boldsymbol{A} = \mu \boldsymbol{\jmath} - j\omega\mu\epsilon \nabla \Phi + \omega^2 \mu\epsilon \boldsymbol{A}. \tag{2.26}$$

Equations (2.25) and (2.26) can be simplified by applying the *Lorentz condition* which states that $\nabla \cdot \boldsymbol{A} = -j\omega\mu\epsilon\Phi$. Thus (2.25) and (2.26) become

$$\nabla^2 \Phi + \omega^2 \mu\epsilon \Phi = -\frac{\rho}{\epsilon}, \tag{2.27}$$

$$\nabla^2 \boldsymbol{A} + \omega^2 \mu\epsilon \boldsymbol{A} = -\mu \boldsymbol{\jmath}. \tag{2.28}$$

Equation (2.28) is known as the *vector wave equation* [6, p. 31], and it can be noted that the term $\omega^2\mu\epsilon$ represents the squared propagation constant β as was defined in

[3] the analysis presented henceforth is conducted for time-harmonic fields and thus the phasor notation.

section 2.1.2. Then, we can express (2.28) as

$$\nabla^2 \boldsymbol{A} + \beta^2 \boldsymbol{A} = -\mu \boldsymbol{\jmath} \tag{2.29}$$

Equation (2.29) can be decomposed into rectangular components, $\nabla^2 \boldsymbol{A} = \boldsymbol{a_x} \nabla^2 A_x + \boldsymbol{a_y} \nabla^2 A_y + \boldsymbol{a_z} \nabla^2 A_z$, and be solved by assigning three scalar equations

$$\nabla^2 A_x + \beta^2 A_x = -\mu \jmath_x, \tag{2.30}$$
$$\nabla^2 A_y + \beta^2 A_y = -\mu \jmath_y, \tag{2.31}$$
$$\nabla^2 A_z + \beta^2 A_z = -\mu \jmath_z, \tag{2.32}$$

A procedure to solve any of these equations is similar since they are of the same form. In order to get there, a solution to a point source will be in the form of a unit impulse response. This will constitute a general solution if we consider an arbitrary source as a set of point sources. The differential equation for the point source will be given as

$$\nabla^2 \psi + \beta^2 \psi = -\delta(x)\delta(y)\delta(z), \tag{2.33}$$

where ψ is the response to a point source and $\delta()$ is the unit impulse response. Taken the point source current as having a z-direction, the response to the point source at the origin becomes $\psi = A_z$, and since the point source will be zero everywhere except the origin equation (2.33) will provide the solution for the waves propagating away from the source when it holds that

$$\nabla^2 \psi + \beta^2 \psi = 0. \tag{2.34}$$

Spherical coordinates can be used now for convenience because ψ depends only on the radius r. Equation (2.34) is a homogeneous differential equation whose two solutions will be $e^{-j\beta r}/r$ and $e^{+j\beta r}/r$. As it was seen in equations (2.18) and (2.19), these solutions represent a pair of traveling waves. We consider only $e^{-j\beta r}/r$, since it is the solution to waves propagating outwardly from the point source. The point source solution (solving for (2.33) when the point source is located at the origin) is given by:

$$\psi = \frac{e^{-j\beta r}}{4\pi r}.$$

This solution provides the magnitude and phase variation with respect to the radius r when the point source is at the origin. In a more general case, the point source may be located somewhere else and a distance R must be calculated between the source and an observation point P.

We are interested in the distance between the point source and the observation

point and thus the solution will be

$$\psi = \frac{e^{-j\beta R}}{4\pi R}. \tag{2.35}$$

A complete solution to the magnetic vector potential will include the sum of all the point source responses enclosed by the source volume v' in all x, y, and z components. Hence

$$\boldsymbol{A} = \iiint_{v'} \mu \boldsymbol{\jmath} \frac{e^{-j\beta R}}{4\pi R} dv', \tag{2.36}$$

which is the solution to the vector wave equation (2.29). So once we know the current distribution $\boldsymbol{\jmath}$, we can obtain the magnetic vector potential A. The magnetic field intensity $\boldsymbol{H}$ can be derived then from equation (2.22), and finally the electric field intensity $\boldsymbol{E}$ can be obtained from the magnetic curl of Maxwell's equations (2.8), that is

$$\boldsymbol{E} = \frac{1}{j\omega\epsilon}(\nabla \times \boldsymbol{H} - \boldsymbol{\jmath}),$$

which solves for the electric fields inside the source region. If the fields radiated away from the source need to be found, $\boldsymbol{\jmath}$ is set to zero at the field point P.

If we are interested in the instantaneous expression of the magnetic vector potential, a solution to the vector wave equation (2.28) will have the form

$$\vec{A}(R,t) = \frac{\mu}{4\pi} \iiint_{v'} \frac{\vec{\jmath}\left(t - \frac{R}{v_p}\right)}{R} dv'. \tag{2.37}$$

The term $t - \frac{R}{v_p}$ indicates that the magnetic potential evaluated at time t from a distance R depends on the value of the magnetic potential at an earlier time, $t - \frac{R}{v_p}$. This is due to the fact that electromagnetic waves travel at a finite velocity of propagation v_p. Therefore, equation (2.37) is referred to as the *retarded vector potential*. This retardation effect can be seen in equation (2.36) as a phase shift of each contributing source point with respect to distance r, and it is indicated by the term $e^{-j\beta R}$. Retardation is a very important concept in the analysis of high-frequency circuits where the size of the circuit is smaller than the operating wavelength.

2.2 Fundamentals of Antenna Theory

A fundamental component of any RF system, antennas play a crucial role in enabling the actual radio transmission/reception of electromagnetic waves. At present, the study and design of ever more complex antenna systems -on handsets, base stations, and measurement instruments- have become mandatory to respond to the

integration and functionality of different cellular technologies across a wide range of frequency bands. This section presents the reader with the basic concepts of antenna theory intended to allow a better understanding of the antenna coupler used in our measurements, as well as the characterization of the near-field regions where measurements will be conducted.

2.2.1 Basic definitions

In the previous section we described how a solution to Maxwell's equations for radiated fields can readily be obtained if we know the current distribution. A magnetic vector potential was introduced and shown to facilitate the solution to the electromagnetic fields. The discussion presented serves to characterize the phenomenon of radiation that occurs when electrons flowing in a conductor are accelerated (decelerated). As such, this radiation may even happen in a simple wire when the latter conditions are met. In some cases, the radiation that arises in wire conductors may cause electromagnetic emissions that interfere deleteriously with other systems, and in general indicate a poor isolation or shielding. On the other hand, radiation may be the actual target in the design of a system and in this case, the radiating structure requires to have certain properties that allow it to radiate the electromagnetic fields efficiently and in a controlled fashion. Such structures have become known as *antenna systems* or simply *antennas*. An antenna is defined as a transition device, or transducer, that allows the transmission of an electromagnetic wave from a guiding structure into free space, or due to its reciprocal nature, an antenna allows the reception of an electromagnetic wave from free space into a guiding structure [6, p.10-11]. A key requirement for an antenna to be an efficient radiator is dictated by its physical size, which should be comparable to the wavelength of the operating frequency [6, p. 11].

It has been mentioned that a fundamental requirement for radiation to occur is that there be a charge disturbance. Even though accelerated (decelerated) charges are necessary for the generation of radiated waves, they are not required for sustaining the radiation [8, p. 10]. Antenna systems are designed to perform according to given specifications, and the antenna performance is evaluated according to a set of parameters. In the next section, these parameters are discussed. Before that, however, the definition of a *decibel* is introduced as it is widely used in the context of radiated power levels and will be often encountered henceforth in this writing.

Decibel

A decibel is a convenient notation used when a ratio of two power levels, P_1 and P_2,

is expressed as

$$10 \log \frac{P_1}{P_2} \quad [dB].$$

This type of notation greatly facilitates the calculation of power loss or gain in link budgets because instead of employing multiplying factors, the computation is reduced to summing or subtracting losses or gains.

2.2.2 Antenna performance parameters

Radiation pattern

The radiation pattern of antenna is one of its most important properties and is defined as the graphical representation of its radiative characteristics in terms of the coordinates used, at a distance r from the origin of the coordinate system where the antenna is placed [9, p. 27]. The quantities usually portrayed in a radiation pattern are the fields or power patterns and they are often normalized with respect to their maximum value. Likewise, it is customary to plot the radiation patterns in a spherical coordinate system as the one shown in Figure 2.1 where the axes belong to the Cartesian (rectangular) system.

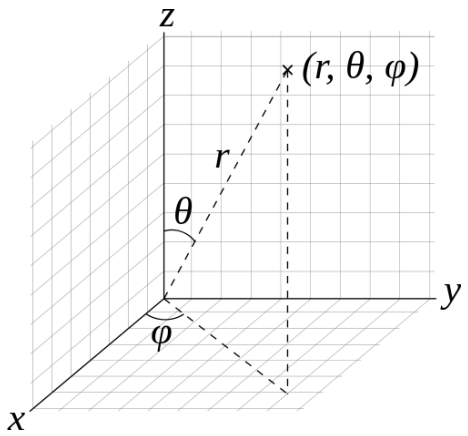

Figure 2.1: Coordinate system to plot antenna patterns. Reproduced from Wikipedia.

A relationship between the two coordinate systems is given by [10, p. 92]

$$r = \sqrt{x^2 + y^2 + z^2}, \qquad \cos\theta = \frac{z}{\sqrt{x^2 + y^2 + z^2}} = \frac{z}{r}, \qquad \tan\phi = \frac{y}{x},$$
$$x = r\sin\theta\cos\phi, \qquad y = r\sin\theta\sin\phi, \qquad z = r\cos\theta.$$

A three-dimensional antenna pattern provides a faithful representation of the radiation properties of an antenna with respect to all the possible values that θ and ϕ can take on. This is indeed a very desirable situation, but in practice it is not easy to obtain such 3D plots nor always strictly necessary. Often, it suffices to present a radiation pattern in a 2D plot where plane cuts are selected to portray the electric

or magnetic field intensities. These planes will lie orthogonal to each other.

Let us illustrate a radiation pattern with an example. Figure 2.2 shows the radiation pattern [4] of an equally spaced 5-element array antenna. The array is designed to reach maximum radiation at $\theta = 90°$. In this example, the radiation pattern is represented in the cut plane where ϕ is fixed, for instance $\phi = 90°$, and the plot is a function of the variation of θ. The radiation pattern is illustrated in polar coordinates and in their rectangular counterparts. The latter can be computed from the equations given above.

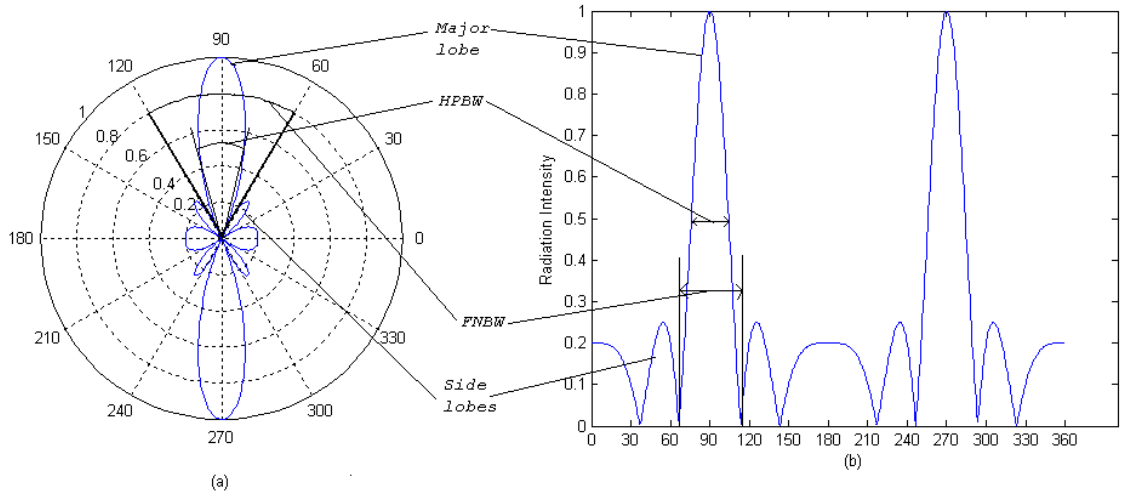

Figure 2.2: Radiation pattern of 5-element antenna array. The cut plane is selected as a function of θ when $\phi = 90°$. (a) Polar coordinates. (b) Rectangular or Cartesian coordinates. Notice that the radiation pattern is normalized to the maximum value of the electric field intensity. Some of the most relevant parameters that characterize a radiation pattern are also shown: main and side lobes, the first null beamwidth (FNBW), and the half power beamwidth (HPBW). These and other parameters are described below.

A radiation pattern has certain parameters that help characterize the radiation properties of the antenna producing that radiation. Some of these parameters are shown in Figure 2.2.

The *major lobe* or *main beam* is defined as the lobe located in the direction where the radiation is maximum. All other lobes are referred to as *minor lobes*. *Side lobes* are identified as the lobes that are adjacent to a given lobe of interest. A *back lobe* lies diametrically opposite to the main lobe. Intuitively, a pair of further parameters are readily observed. The *Half-power beamwidth* ($HPBW$) is defined as the region limited by the angular separation of the points where the power level is half of the maximum radiated. Finally, a *First-null beamwidth* ($FNBW$) is defined as the region confined by the angular separation between two lines that are tangent to the

[4] In fact, Figure 2.2 represents the array factor of the antenna. However, by assuming that each array element is an isotropic radiator with no angular dependency, the array factor and the radiation pattern are the same [11]

points where the main lobe and its respective sidelobes intersect. These points are referred to as the first nulls.

Radiation patterns are usually defined for regions where the electromagnetic fields have very similar properties to those of a plane wave. This region is referred to as the *far-field* or *Fraunhofer* region. A key characteristic of this region is that the wave impedance of the electromagnetic field equals the intrinsic impedance of free space. However, radiation patterns and other antenna parameters can also be evaluated in a region inside the far-field known as the *near-field* region. This region can be divided into two sub-regions: a *reactive near-field* region and a *radiating (radiative) near-field* or *Fresnel* region. The former is characterized by the predominance of the reactive fields over the radiating (real) fields, while the opposite holds for the latter. Figure 2.3 illustrates all the above regions.

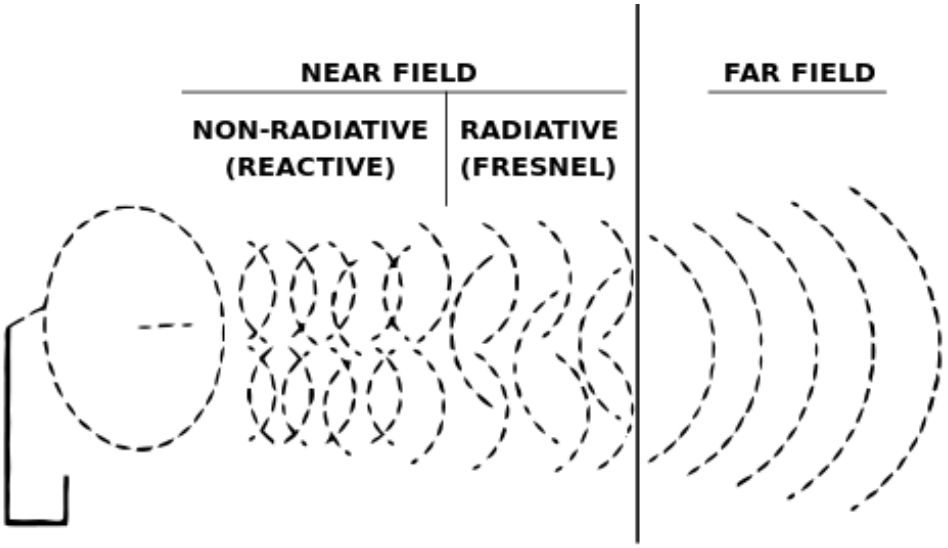

Figure 2.3: Radiation field regions. Reproduced from Wikipedia.

Electrically small antennas are antennas whose dimensions are very small compared to the operating wavelength, in particular for the low frequency bands. By defining the largest dimension of the antenna structure as D, a convention in [6, p. 43] establishes that for electrically small antennas $D/2 \ll \lambda$, while electrically large antennas are defined by $D > 2.5\lambda$. Radiated RF measurements are often conducted in the radiating near-field or far-field regions where the radiating (radiative) fields are preponderant, although as it will be shown in our study, accurate results are also achievable in the reactive near-field region. Field regions are defined for electrically small and large antennas. Although not exact values, there are ranges commonly used and represent a good approximation. These field ranges are summarized in Table 2.2 [9, p. 34]. R_1 represents the boundary confining the reactive near-field region, whereas R_2 encloses the radiating near-field region and marks also the beginning of the far-field.

Table 2.2: Field region boundaries defined for electrically small and large antennas.

Electrically small antennas	**Electrically large antennas**
$R_1 = \frac{\lambda}{2\pi} = 0.16\lambda$	$R_1 = 0.62\sqrt{\frac{D^3}{\lambda}}$
$R_2 = 5\lambda$	$R_2 = \frac{2D^2}{\lambda}$

Antenna impedance and radiation efficiency

As in any other conventional circuit, an input impedance can be defined for an antenna. An antenna impedance is a complex-valued parameter which can be denoted as

$$Z_A = R_A + \jmath X_A, \tag{2.38}$$

where R_A represents the real part and X_A the imaginary or reactive part. The real part comprises two components: a radiation resistance R_r accounting for the power dissipated in the form of intended radiation, and a resistance that takes into account the power dissipated in the form of ohmic losses and denoted as R_o; thus $R_A = R_r + R_o$. A radiation efficiency of an antenna is defined as [6, p. 60]:

$$e_r = \frac{R_r}{R_r + R_o} = \frac{R_r}{R_A}.$$

One of the fundamental factors that affects an antenna efficiency is the losses due to an impedance mismatch at the antenna input terminals. A voltage reflection coefficient, Γ, exists at the interface of a transmission line (connected to the antenna) and the antenna input terminals, and is defined as [9, p. 65]

$$\Gamma = \frac{Z_{in} - Z_o}{Z_{in} + Z_o}, \tag{2.39}$$

where Z_{in} represents the input impedance of the antenna, and Z_o is the characteristic impedance of the transmission line. A more common parameter that also quantifies the level of impedance mismatch is the voltage standing wave ratio and given as [9, p. 65]

$$VSWR = \frac{1 + |\Gamma|}{1 - |\Gamma|}. \tag{2.40}$$

Values of VSWR range from 1 to ∞, the former for a complete impedance matched case, that is when $Z_{in} = Z_o$, and the latter for a total mismatch when the interface is a shorted or left opened and all the power is reflected back at the interface.

Antenna polarization

The polarization of an antenna directly refers to the polarization of the wave that is being radiated by the antenna, and in particular the plane wave in the far-field.

The polarization of plane waves was introduced in section 2.1.2, and the same principles apply to the present discussion. The polarization of the waves radiated by the antenna depends on the angle it is evaluated at. If no such angle is specified, it is commonly assumed that the polarization corresponds to that of the main beam. In the main beam, the polarization characteristics of an antenna are usually constant. In the side lobes, on the other hand, the polarization can vary significantly. Analogous to its radiation pattern, an antenna can be characterized by its polarization pattern which is defined as the spatial distribution of the polarizations generated by the antenna over its radiation sphere [9, p. 72]. The magnitude and relative phase of two orthogonal components, E_θ and E_ϕ, are commonly used when measuring the polarization of an antenna. These components allow us to define some principal planes patterns. In case of linearly polarized antennas, the principal plane patterns are completely specified by measuring the E_θ-component in the E- and H-planes [6, p. 65]. In other words, the E_θ and E_ϕ components describe the *co-polarization* and *cross-polarization* of the antenna, respectively. Since the E- and H-planes are not uniquely specified for circularly polarized antennas, the principal planes in this case have to be defined with respect to some fixed direction, often chosen as the $\phi = 0°$ and $\phi = 90°$ planes. A circularly polarized antenna can be right-hand or left-hand polarized.

Due to their reciprocal nature, antennas are said to be polarization matched if they have the same polarization both on transmit and receive. Therefore, a receive antenna will successfully detect a wave radiated by a transmit antenna if both have the same polarization.

2.3 Basics of Statistics and Process Capability Analysis

The present section describes the statistical methods applied in this thesis to the measurement data. These are fundamental tools used for the analysis of output data in any process where the goal is not only to characterize the process itself as accurately as possible, but most importantly to implement quality and productivity improvement and process optimization when needed. Any statistical analysis starts with the selection of a subset of data from a population known as a sample. A population is a set of items or events from which a given parameter may be evaluated. A population must represent all the possible realizations of a process within a certain frame [12, p. 59]. The sampling process facilitates the analysis of the data in that only a random subset of data, representative of the whole population and its variations, can be used to accurately characterize the entire population and examine a given parameter. If the sampling is random and large enough, factual generalizations can be made about the entire population, resulting in a time-and-cost saving process [12, p. 59].

A fundamental assumption in a statistical capability analysis, as presented in this thesis, is that the process under scrutiny should be in control. A process is said to be in control if it is subject to a constant system of variability causes [12, p. 68]. This type of variation is often considered as random variation, is present in every process and is generated by the process itself. A second type of variation, that of a special cause origin, makes the process unpredictable since it is caused by unique disturbances that may be a one-time event or appear as a permanent process change. The following example will elucidate these concepts. A production line that produces a given set of items per day will experience a variation of the output number obtained at the end of the day, that falls within a predictable range. Thus, this number may vary within a specified ± standard deviations with respect to the average number that is produced on a daily basis. In this case, the system is subject to predictable variations (delay from suppliers, short halts in the production line due to maintenance, etc.). On the other hand, a severe machine breakdown or power outage that would cause a significant drop in the production output represent a variation of special cause origin. The measurement results presented in this thesis obey solely to variations of a common cause nature, and the process is thus in control. A couple of examples presented in the next section will illustrate this.

Let us further explore some important concepts of the theory of probability and probability distribution. This will enable a better understanding of the capability process analysis studied in this thesis.

2.3.1 Basic concepts in probability and normal distribution

Probability theory is the branch of mathematics that is concerned with the construction, analysis and interpretation of probability models of random occurrences. A random experiment is a process that results in any of several possible outcomes in a trial [12, p. 69]. The actual occurrence of a given outcome on a certain trial cannot be predicted with absolute certainty. A series of trials of a random experiment can be conducted under identical conditions and the result is a distribution of experimental data. Probability theory is the tool per excellence to analyze and interpret such data.

Let us assume that a random experiment is conducted and yields a total of n possible different outcomes, A_i, i=1, 2, 3....., n. If m trials of the experiment yielded the outcomes A_1, A_2, ..., A_n, which occurred m_1, m_2, ..., m_n times, the probability of the outcome A_i can be estimated by [12] by

$$p_i = \frac{m_i}{m}, \qquad i = 1, 2, 3, ..., n.$$

Because $m_i \leq m$,

$$0 \leq p_i \leq 1, \qquad i = 1, 2, 3, ..., n. \tag{2.41}$$

and $m_1 + m_2 + \cdots + m_n = m$, we conclude that

$$\sum_{i=1}^{n} p_i = 1. \tag{2.42}$$

Equations 2.41 and 2.42 constitute two fundamental laws of probability. The former states that a probability can only assume values ranging from 0 to 1, while the latter asserts that the sum of the probabilities of all possibles outcomes is equal to exactly 1. A *random variable* is an outcome or individual observation that varies randomly, as opposed to deterministic variables whose outcomes are known beforehand. The output of a random variable can only be determined statistically. Two types of random variables can be distinguished. A *discrete random variable* is a variable that can assume only a finite (integer) value. An example of a discrete random variable is the amount of broken bulbs that are set aside from a batch of new bulbs that have been manufactured. By contrast, a *continuous random variable* is a random variable that can theoretically assume an infinite number of values within a specified interval, although in reality measurement instruments set constraints on the number of decimal places in the measurements [13]. Examples of a continuous random variable are temperature, voltage, or pressure measurements. In this thesis we will only be concerned with continuous random variables and the remaining of the analysis in this section pertains to this type of variables. An important rule of two outcomes or events is related to their independence of occurrence. Two events, A and B are said to be independent if the occurrence or non-occurrence of one of them has no effect on the probability of occurrence of the other and the notation used to indicate this independence is

$$P(A \textit{ and } B) = P(A \cap B) = P(A)P(B).$$

When the outcome of a probability is a compound outcome having two or more events the probability is called *joint probability*, and it can be expressed as [12]

$$P(A, B) = P(B|A)P(A), \tag{2.43}$$

where the term $P(B|A)$ denotes a *conditional probability* because a condition, A, is specified or imposed on event B. Equation 2.43 is known as the *multiplication law of probability*. The term $P(B)$ is referred to as the marginal probability of the

outcome. In turn, the *addition law of probability* is defined by

$$P(A+B) = P(A) + P(B) - P(A,B). \tag{2.44}$$

A special case of Equation 2.44 occurs when two events are mutually exclusive, that is they cannot occur simultaneously. In such case, 2.44 is reduced to

$$P(A+B) = P(A) + P(B).$$

The above properties can be expanded to more than two events as shown in [13, p. 73].

Once an experiment is conducted and a set of outcomes obtained, it is necessary to represent such data in such a way that statistical parameters can easily be inferred and analyzed. Statistical distributions are the most common way to do that and they are also known as *probability distributions*. Continuous random variables are represented by a continuous probability distribution known as the *probability density function* or *probability distribution function*, (pdf). A formal mathematical definition [14, p. 57] states that a random variable X is continuous if for some function $f : \mathbb{R} \to \mathbb{R}$ and for any numbers a and b with $a \leq b$,

$$P(a \leq X \leq b) = \int_a^b f(x)dx.$$

The function f has to satisfy the condition $f(x) \geq 0$ for all x and $\int_{-\infty}^{\infty} f(x)dx = 1$. The function f corresponds to the pdf of X.

One of the most important probability distribution functions is the normal distribution. Prior to discussing this kind of distribution, it is helpful to explain the most relevant metrics used to characterize such distribution. In addition to the random variable X under observation, let us denote N as the sample size.

We begin with the population *mean*, or the *true arithmetic mean* value of X and is given as

$$\mu = \frac{\sum_{i=1}^{N} X_i}{N}.$$

Another important statistical parameter is the *variance*. The variance is a measure of the dispersion of the data set or distribution as it is scattered around the population mean. Quantitatively, the variance is given by

$$\sigma^2 = \frac{\sum_{i=1}^{N} (X_i - \mu)^2}{N}.$$

The variance is an essential parameter that is monitored in quality control procedures. A manufacturing process, for instance, will see a decrease in failed outputs and an increase in precision if the variance is reduced. Because the variance is a squared quantity, a more convenient way to express the same measure of data dispersion is by applying the square root to the variance σ^2, yielding what is known as the *standard deviation* and is given by

$$\sigma = \sqrt{\frac{\sum_{i=1}^{N}(X_i - \mu)^2}{N}}.$$

Notice that the standard deviation has the same units as the data being observed and that is the reason why it is more commonly used. Let us consider next the normal distribution.

Normal Distribution

A normal distribution or Gaussian distribution is used to approximate the actual distribution of many natural and man-made phenomena. The normal distribution is defined mathematically by the equation [13, p. 93]

$$f(x) = \frac{1}{\sigma\sqrt{2\pi}} e^{-(x-\mu)^2/2\sigma^2}, \qquad -\infty < x < \infty.$$

The infinite range set to x denotes the fact that as a continuous random variable, it can assume any real number. Typically, any normal distribution is characterized by its mean and standard deviation metrics.
Figure 2.4 illustrates three normal distributions whose data present a single population mean value around which, three different standard deviations result in three levels of data dispersion as shown.

The value of the standard deviation σ determines the shape of the distribution, while the value of the mean μ dictates its location [13]. The total area under $f(x)$ equals to one, which correspond to the total probability of one, with a probability of 0.5 on each side of the population mean μ. Figure 2.5 illustrates an example of a normal distribution with different areas demarcated by three standard deviations on each side of the mean μ. We will see that six standard deviations account for almost the whole of the variation present in a distribution and the capability of a process is calculated in terms of these six standard deviations. Likewise, control charts used to evaluate the causes of variability of a process set their control limits at $\pm\ 3\sigma$.

A very useful graphical tool to assess whether or not a data set is reasonably characterized by a normal probability distribution is the *normal probability plot*. They are especially useful in identifying any possible outlying data in a sample

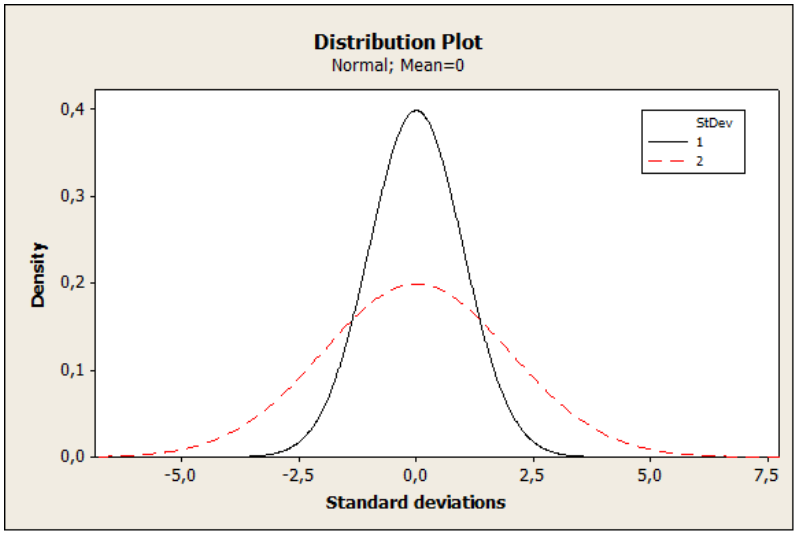

Figure 2.4: Two different normal distributions with the same mean and distinct standard deviations. Plot made with Minitab®16 [15].

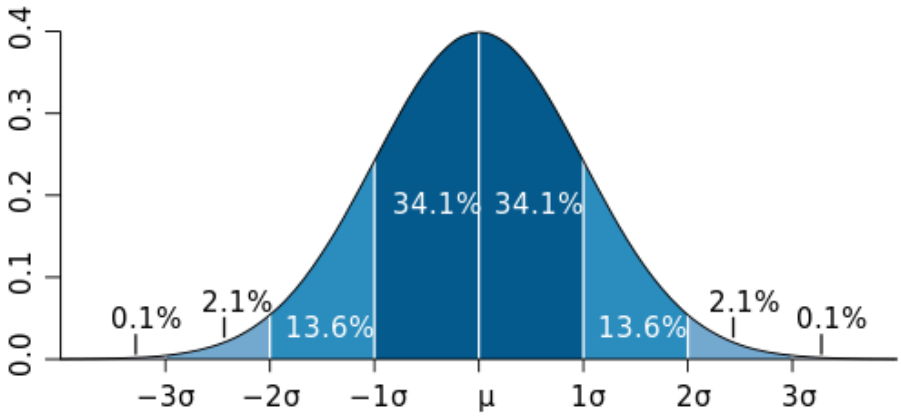

Figure 2.5: Areas under a normal distribution with outer limits set at $\pm 3\sigma$. Reproduced from Wikipedia.

population. A normal probability plot portrays the cumulative probability on the vertical axis and the value of a given variable on the horizontal axis. A straight line aids in the measure of normality. Each data point from the distribution is plotted at its unique coordinate and the normality is evaluated by observing how much each data point digresses from the straight line. If all the data points appear to be distributed along the straight line, and the latter passes on (or near) the intersection of the mean and 50% probability, then the data may be considered to be in good normality [12, p. 93]. When the plot of the data points exhibits a pronounced S-shaped, on the other hand, the normality of the distribution should be suspected. We will include normal probability plots in our analysis of the measurement results in chapter 4. An example of the normal probability plot drawn for the output power in GSM 850 is shown in Figure 2.6.

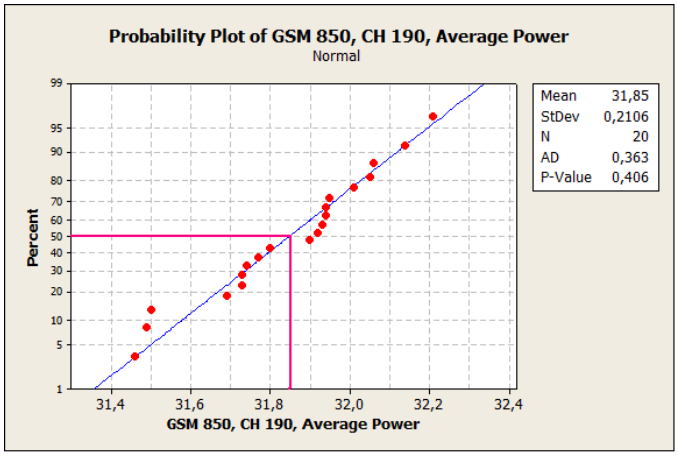

Figure 2.6: Normal probability plot of output power in GSM 850, CH 190. Plot generated with Minitab®16 [15]. Note that the scales are automatically adjusted by the software so that the probability distribution becomes a straight line. Notice the intersection of the 50% probability and the mean. Also, the data points are fairly distributed along the straight line. A normal distribution, then, can be inferred from the plot. Values to consider on the upper right box shown are the mean value (Mean), standard deviation (StDev), and the number of samples (N). Not relevant for the present thesis, (AD) refers to an Anderson-Darling statistic that measures how well the data fit several distributions, while (P-Value) is the probability of obtaining a test statistic that equals the calculated value if a null hypothesis holds true (a null hypothesis is one of the statements that results from a test run on two mutually exclusive statements about a population).

Control Charts

It was mentioned above that a process should be in statistical control before a meaningful process capability analysis can be performed. Control charts diagrams have become a powerful tool in quality control processes. Statistical control on continuous random variables is evaluated with variable charts known as $\overline{X}$ and R charts and moving range MR charts. The former are used for high volume sampling while the latter for low volume [16]. High volume sampling is defined as a process where 100 measurements are made, divided into three periods so that in one period 50 samples are taken and 25 samples in the other two. Low volume sampling, on the other hand, is comprised by 10 consecutive samples [16, p. 146]. For our measurements, as it will be shown in Chapter 4, we have selected 20 [5] samples to conduct the capability analysis, so for the examples presented next we use $\overline{X}$ and R charts to assess the level of statistical control. The parameters shown in the charts

[5] In principle, 100 measurements are recommended for a high-volume process, although the same author proposes that 30 samples can be used for the said process [16, p. 146]. However, [17] states that a minimum of 20 samples is enough to conduct a process capability analysis. My measurements support the latter claim and a sample size of 20 samples will be sufficient to run a consistent control check and subsequent process capability analysis, as data from chapter 4 will demonstrate.

are calculated as follows [12, p. 155 - 156]:

$$\overline{X}_i = \sum_{j=1}^{n} X_{ij}/n,$$

yields the mean, where X_{ij} is the jth measurement, $j = 1, ..., n$, in the ith sample and the sample size is given by n. The range measures the spread within the ith sample and is given as $R_i = X_{largest} - X_{smallest}$. A so called grand range, $\overline{\overline{X}}$, is defined as the arithmetic average of all the available sample averages and thus given as:

$$\overline{\overline{X}} = \frac{\sum_{i=1}^{k} \overline{X}_i}{k},$$

where k is the number of samples that are used to set up the control chart. In turn, the average of the sample ranges is given by

$$\overline{R} = \frac{\sum_{i=1}^{k} R_i}{k}. \tag{2.45}$$

Figure 2.7 shows the control charts for the output power of GSM 850, with 20 samples measured. The upper and lower control limits, (UCL) and (LCL), are displayed 3 standard deviations above and below the center line and they represent the actual amount of variation that is expected from the process based on the sample data. The control limits for the the $\overline{X}$ chart are calculated as follows [16, p. 74-75]:

$$UCL(\overline{X}) = \overline{\overline{X}} + 3\sigma = \overline{\overline{X}} + A_2 \cdot \overline{R},$$
$$LCL(\overline{X}) = \overline{\overline{X}} - 3\sigma = \overline{\overline{X}} - A_2 \cdot \overline{R}.$$

As for the control limits for the $\overline{R}$ chart,

$$UCL(\overline{R}) = \overline{\overline{X}} + 3\sigma = D_4 \cdot \overline{R},$$
$$LCL(\overline{R}) = \overline{\overline{X}} - 3\sigma = D_3 \cdot \overline{R},$$

where the control limit factors A_2, D_3 and D_4 are constants found in control chart factors Tables, such as [16, p. 75].

Let us also see how the measurements conducted for 150 samples fare in their statistical control test. Figure 2.8 illustrates the control charts made for the 150 samples in GSM 850, output power.

In both Figures, only half of the samples are represented as the minimum number of subgroups allowed in Minitab is 2. Both processes are manifestly in statistical

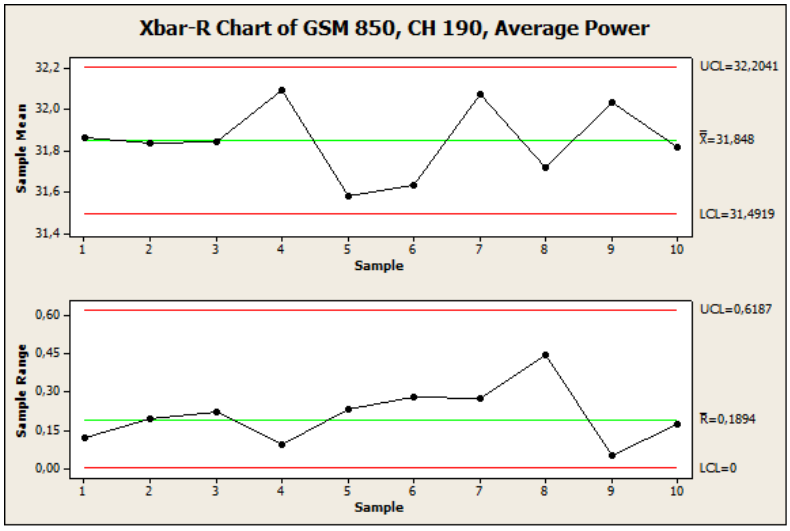

Figure 2.7: $\overline{X}$ and R charts for output power in GSM 850. 20 samples were measured. Plot generated with Minitab®16.

control because all of the samples are confined within the control limits, [12] and [16]. When we present the measurement results in Chapter 4, only will the process capability and normal probability plots be included. The control charts just described have been calculated for every RF performance parameter evaluated in this thesis and because the same compliance has been observed throughout, no additional control charts are included henceforth.

2.3.2 Process capability assessment

The foregoing discussion underscored the importance of having a process under statistical control as a prerequisite to the proper assessment of its performance as measured by the process capability. Control charts are used to assess the statistical control of a process, but they cannot be used to assess the conformance of a process to some quality/safety specifications. The reason for this is because from a statistical point of view, conformance to specifications implies the process as a whole and the attention is focused on the distribution of individual measurements, whereas statistical control relies on summary statistics from each sample, and thus the distributions observed deal with this type of statistics and not with that of individual measurements [12, p. 256]. A process capability analysis serves to evaluate how good a process is to conform to a set of specification limits. In other words, it is a metric that exposes the performance of a process in terms of given quality characteristics being tested. Having a process under statistical control does not guarantee conformance to specifications. This may be the case when, for instance, the process is not centered properly [12]. The specification limits used for process capability assessment of the different RF parameters are characteristic of each phone

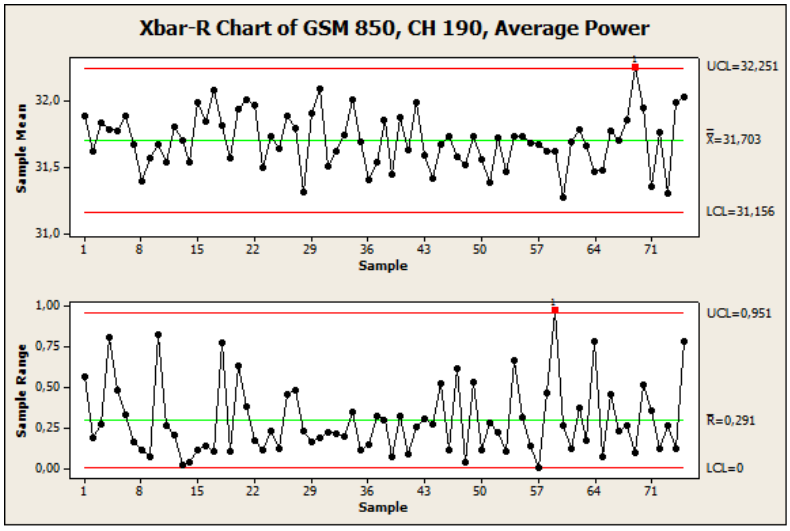

Figure 2.8: $\overline{X}$ and R charts for output power in GSM 850. 150 samples were measured. Plot generated with Minitab®16.

being tested, and they are based on functional considerations. The process capability assessment, in the present thesis, will establish a phone´s conformity to design constraints and 3GPP specifications. In order to assess a process capability, some indices are used to quantify the level of conformance to specification limits. The two most important indices are Cp and Cpk.

Process capability Index (process potential), Cp

Products are manufactured using materials and processes that vary within given tolerances. Designs are made so that the characteristics of materials and processes are specified to nominal values. The maximum range of variation of the product characteristic gives the tolerance of the nominal values. Upper and lower specification limits, (USL) and (LSL), provide the range of that tolerance [16, p. 36], and they are based on customer requirements and indicate the amount of desired variation (as opposed to control limits that, as was mentioned above, display the actual variation extracted from sample data). The process capability is defined as the full range of variation that a manufacturing process undergoes, when a given parameter is measured. Processes with a normal distribution have 99.73 % of their output lying between $\pm$ 3σ with respect to the mean μ [16]. Thus, the process capability index Cp is given by [12]

$$Cp = \frac{USL - LSL}{6\sigma} \tag{2.46}$$

Cp is called the *process potential* in some literature. It relates the process capability, six standard deviations, to the design specifications range. It does not involve the location of the process with respect to the specification limits [18]. The minimum acceptable value for Cp is said to be 1 [12, p. 265]. Values of Cp exceeding 1.33 are indicative of a process being adequate to meet the specifications. Values

ranging from 1.33 and 1 indicate that even when the process is able to meet the specifications, it will require close control [18].

Process capability Index, Cpk

Cpk is an index that has become very popular since it is a capability index that relates the process mean to the nominal value of the specification [12]. Cpk indicates how a process fares with respect to its specification limits, and is calculated as [12, p. 266]

$$Cpk = min\left[\frac{USL-\mu}{3\sigma}, \frac{\mu-LSL}{3\sigma}\right] \tag{2.47}$$

Cpk is a metric that measures how far the process mean is from the design specification limits in terms of 3σ ranges [18]. The 3σ range shift is observed in the denominators of Equation 2.47. A very common quality control method known as Six Sigma is used in the industry and it specifies a process capability of Cp=**2** and Cpk=**1.5** [16, p. 44]. These Cpk values are the process capability indices that we will aim at in our analysis of the RF radiated measurement results presented in Chapter 4.

Process performance Pp, PpK

In addition to the process capability indices, Pp and PpK are indices that measure the performance of a process from the customer perspective [18]. Process capability measures the ability of a process in a short term. Process performance, on the other hand, is considered in some literature to measure the long term ability of a process to conform to the specifications. A clear distinction is made between a process capability and a process performance whereby the latter uses the overall standard deviation and not a short term estimate of the standard deviation as is attributed to the former [18].The overall standard deviation is a weighted average that accounts for the variation of within-group and between-group. These are subgroups of units produced under the same set of conditions. *Within subgroups* refer to common cause variation, whereas *between subgroups* account for special causes of variation. Minitab®16 [15] identifies the process performance indices Pp and PpK as the overall capability of the process as it accounts for differences between subgroups. When we calculate the capability indices on our measurement results in Chapter 4, the overall capability indices will be shown since in practice, they correspond to the process capability metrics given by Equations 2.46 and 2.47. The reason for this is because our measurement system does not contain any special cause variation, and the capability indices are in fact given by the said equations. In keeping with this convention, our analysis of the measurement results in Chapter 4 will allude to Cp and Cpk indices, even when the Figures will show Pp and PpK indices.

3. MEASUREMENT SYSTEM ANALYSIS

This chapter presents a study of the test system used to conduct the measurements analyzed in this thesis. In any measurement, a reliable test system is required to obtain a level of accuracy that can ensure that the physical phenomenon or quantity being tested is duly characterized and quantified. This is accomplished by conducting proper and regular calibration of the test instruments, eliminating or at least minimizing any sources of error, and when the latter become unavoidable, they should be accounted for in the analysis of the test results. Furthermore, in certain measurements such as the ones underlying this thesis, a repeatability factor plays a fundamental role in the successful outcome of accurate and reliable results owing to the statistical analysis extracted from the measurements.
Radiated measurements give rise to uncertainties that are proper to the radio environment where the test is conducted. Given the dimensions of commercial RF shield boxes, reflections inside the box and errors due to complex reactive near-field testing represent the main source of uncertainty. The concept of sweet spot will be introduced and in plain terms is defined as the ideal spot inside the RF shield box where the measurements are to be made. This will include the criteria followed to find the sweet spot. Next, we begin our discussion by describing the measurement system.

3.1 Description of Measurement System

The test system is made of three main components, namely: a radio communications tester whose main functions are to simulate a base station and to measure the actual parameters of interest on the mobile phones; an RF shield box where the phone is placed. This box incorporates an antenna coupler that senses the fields radiated by the phone and also serves as the transmitting antenna of the base station simulator. The RF shield box and the radio communications tester are connected using a high-performance coaxial cable. Finally, a PC is used to control the radio communications tester and the two are connected via a GPIB connector. Figure 3.1 shows a diagram of the measurement setup just described.

As it is seen the measurement system is rather simple and yet, it demands great care in guaranteeing a set of conditions conducive to achieving accurate and reliable results. Commercial radio communication testers or base station simulators are very

sophisticated devices that are carefully made and are routinely calibrated, so errors originating from any malfunctioning from these devices are rather uncommon. In turn, RF shield boxes are made to ensure a level of isolation and noiseless environment where measurements are made on the signals coming from the device under test and not on those interfering signals in the surroundings. A laptop controls the radio communication tester using a software from the latter's manufacturer. The measurement system is completed by a GPIB-USB connector and a high-performance flexible coaxial cable (with Navy Type N connectors on its ends) capable of operating at very high frequencies with low levels of attenuation. The latter connects the radio communication tester to one port of the RF shield box. Inside the RF shield box, a conventional thinner coaxial cable (SMA connectors on each end) connects the antenna coupler to the port of the RF shield box.

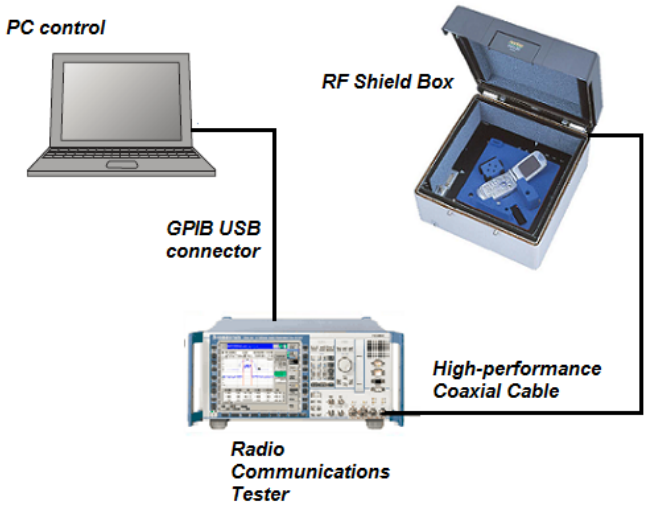

Figure 3.1: Block diagram of measurement setup used to conduct radiated measurements.

Let us see a more detailed description of our measurement setup.

3.1.1 Radio Communication Tester

Radio communication testers are widely used in the mobile communications industry. They are multi-system test platforms that are used to diagnose failures and to evaluate all the main transmission and reception parameters on mobile phones. They typically cover all of the main cellular technologies (GSM, WCDMA, LTE), and in some cases they may include additional wireless technologies capabilities as Bluetooth, GPS, or WLAN, bringing a frequency range coverage of 30MHz to 6GHz.

In order to support all the above features, radio communication testers come with a set of RF generators, RF analyzers, power meters, and spectrum analyzers. RF generators provide a configurable RF signal for test purposes; all the main network

standards are supported for most of the modern radio communication testers, and since the RF signals they generate are simulating those of a real base station, the testers may be referred to as base station simulators in some literature, e.g. [19]. RF analyzers, power meters and spectrum analyzers evaluate different transmitting and receiving characteristics on mobile phones as it will be expatiated upon in Chapter 4. These parameters are evaluated automatically by the radio communication tester by means of a control software. Manual measurements, however, were used to calculate the path loss incurred by the cables, connectors, and the antenna coupler present in the RF path between the radio communication tester and the phone under test. These attenuation values are very critical to the accuracy of the measurement readings and a later discussion will elaborate on the topic.

3.1.2 RF Shield Box

RF shield boxes are enclosures designed to provide RF isolation to the device under test placed inside them from the outer environment. Such isolation is crucial for radiated measurements to be reliable and accurate. RF isolation ensures that the power radiated by the phone under test is directed to the antenna coupler inside the RF shield box and then is conducted through the RF coaxial cable to the radio communication tester. In this way, neighboring test stations or phone users are not affected by the transmitted power of the phone that, incidentally, is set to maximum for diverse test purposes. In a similar fashion, in the absence of an RF shield box neighboring test stations, phone users, or base stations transmitting at high power levels would render a receiver sensitivity measurement performed on the phone under test an impossible task.

RF shield boxes typically come in rectangular shapes. Figure 3.2 shows some commercial samples from different manufacturers. The performance of RF shield boxes is mainly quantified by a figure of merit known as the *shielding effectiveness (SE)*. This figure of merit is a measure of the amount of RF isolation provided by the box and can be defined as [20, p. 16]:

$$SE = R + A + B$$

where R represents the first reflection loss that occurs when the incident energy coming from outside the box is reflected by the surface of the shield box due to the impedance discontinuity of the air-metal boundary. It may happen that not all the incident energy is successfully reflected, and part of it continues to travel through the shielding wall. This energy is attenuated as it travels across the shield by being turned into heat energy. This absorption is denoted by A. Finally, if part of the incident energy reaches the inner wall of the shield it will be reflected by a

new impedance discontinuity from the metal-air boundary. This reflection loss is accounted for be the term B. Typical values of shielding effectiveness, as stated in the datasheets of different manufacturers, range from 50dB to over 80dB. They start to decay as the operating frequency increases.

Figure 3.2: Typical commercial RF shield boxes.

RF shield boxes are readily modeled as a cavity resonator that is excited at certain resonant frequencies. Analytical studies, such as [21] and [22] , have investigated the reflectivity level and electric field distribution inside RF shield chambers. The case studies presented therein are for chambers of larger dimensions than the RF shield box used in this thesis. However, it is reasonable to apply a similar analysis in a smaller scale for RF shielded boxes where the shape remains the same and the resonant frequencies vary as a function of the dimensions as suggested in [23]. In the study presented in [21], the expressions derived from integral-based equations are used to calculate the electric field at different points inside the RF shielded chamber. The results presented in the study underscored an interesting property of RF shield boxes: at frequencies lower than the lowest resonant frequency (in [21], $f_{100} = 45.45$MHz), the electric field is distributed across the chamber with a small variation, around 1 [V/m]. As the operating frequency is increased and exceeds the resonant frequency, several peaks start to appear with a maximum of almost 150 [V/m] at 1GHz. Thus, the operating frequency is a crucial factor that dictates the dimensions of RF shield boxes. Likewise, as it can be expected from a cavity resonator, standing waves are present in an RF shield box. RF absorbers are designed to attenuate the reflections coming from the walls and as a result, the standing waves are significantly mitigated. RF shield boxes are made with RF absorbing lining covering the walls for that very purpose. Standing waves are one of the major source of uncertainty in radiated measurements and one of the major targets when designing an RF box or chamber is to eliminate them [1]. In the RF shield box used

[1]Reverberation chambers represent an exception to this statement. Indeed radiated measurements are conducted inside reverberation chambers, but the approach is different. A reverberation chamber is a metal cavity that has no RF absorbers and where many cavity modes can be excited

in our measurements, it was determined that an additional layer of RF absorber was needed at the bottom of the lower case of the box in order to further attenuate the reflections coming from that part of the box. In fact, without that additional lining it was not possible to obtain accurate results as the power levels measured varied erratically by almost 10dB . The RF absorber employed was a carbonyl iron loaded urethane rubber, which provided from 10dB to 15dB of attenuation across the test frequencies of interest. As mentioned above, another important component incorporated in the RF shield box is the antenna coupler. The next section describes this component in more detail.

Antenna Coupler

RF shield boxes should be able to perform two tasks: it should capture the electromagnetic energy radiated by the phone or antenna under test, and then guide that energy along a transmission line to the radio communication tester. Secondly, it should guide the energy in the opposite direction, that is, from the radio communication tester to the phone under test. Antenna couplers perform such tasks . Although the concept of coupling also includes inductive and capacitive forms, it is the antenna coupling the preferred choice due to the advantages it carries over the other two. For instance, inductive coupling attained with a coil needs preferably an external stick antenna on the mobile phone to achieve accurate measurements. The current trend of compact, integrated antennas on phone units render this method obsolete. Capacitive coupling is done by placing a capacitive coupler opposite to the antenna area of the phone. For an optimal capacitive coupling, the two areas should be of roughly the same size. As the distance between these collocated areas decreases, the antenna impedance is loaded and energy reflections occur in the proximity of the coupling areas causing measurement errors [24]. In antenna coupling, on the other hand, a sensing (coupler) antenna is collocated opposite to the mobile phone antenna. The use of antenna coupling might have been challenged by the fact that narrowband antennas used to be the predominant choice for antenna couplers. Thus, testing of different cellular frequencies (GSM, UMTS, LTE) made the design of different antenna couplers fitting inside an RF shield box a cumbersome task. However, the current trend is to use single wideband antenna structures that allow seamless measurements on a wide range of frequencies. The antenna coupler inside our RF shield box is a spiral antenna covering a frequency range from around 800MHz to 6GHz. Spiral antennas are circularly polarized radiators with relatively constant input impedance and radiation patterns over wide frequency ranges. They are part of a category known as frequency-independent antennas. Some of the funda-

for a given frequency. An average power level is calculated by measuring a transfer function for several stirred positions and averaging those levels [25].

mental properties of these antennas are the *self-complementary* and *angle emphasis*. Self-complementarity is derived as an extension of Babinet's principle of optics by which a source of light behind complementary thin conducting sheets produces lit regions on the source-free side when they are superposed [6]. This leads to an analysis whereby the input impedance of self-complementary antennas is a constant of $185.5 \simeq 60\pi\Omega$ (note that this is not the impedance at the connecting port of the antenna coupler). The angle emphasis property states that frequency-independent antennas are dependent on the angular variation rather than the finite sizes of the antenna elements. Further properties and characteristics of spiral antennas can be found in [9] and [6]. A parameter included in the data sheet of the antenna coupler that highlights the wideband nature of the antenna structure is the voltage standing wave ratio (VSWR). VSWR is a measure of the level of impedance mismatch. Figure 3.3 shows a typical VSWR of wideband antennas such as the antenna coupler built into the RF shield box.

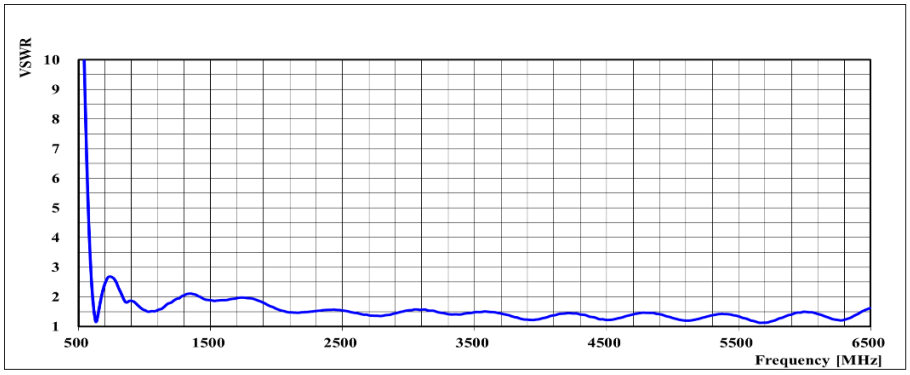

Figure 3.3: Typical VSWR response of frequency-independent antenna structures.

Finally, it is worth mentioning a few words about the baluns in antenna couplers. [6] states that wideband antennas such as the spiral variety are balanced structures. They are, as it is in our case, typically connected to unbalanced structures such as coaxial cables. Therefore, a balun ought to be used in the feeding cable. Both a balun and a wideband load matching structure are, then, reasonably assumed to be incorporated in the compact module of our antenna coupler [2].

The antenna coupler is situated at the very center of the RF shield box in order to facilitate the testing of different sweet spots. A power measurement at different positions of the RF shield box has been conducted with an active phone for the GSM 850 and GSM 1900 bands. The phone was positioned over the plate that held the antenna coupler (reactive near-field sub-region), at different locations: starting from the upper left corner and shifting the positions [3] by 1.2cm, both to the right

[2] Based on our study this is presumed because such data was not available. However, as indicated in [26], modern spiral antennas incorporate balun structures to deal with imbalancing currents.

[3] this was the distance between pin holes on the plate, used to hold the phones fixed at a given

direction and then down, until the whole bottom area of the RF shield box was covered. Figure 3.4 shows the three-dimensional power distribution.

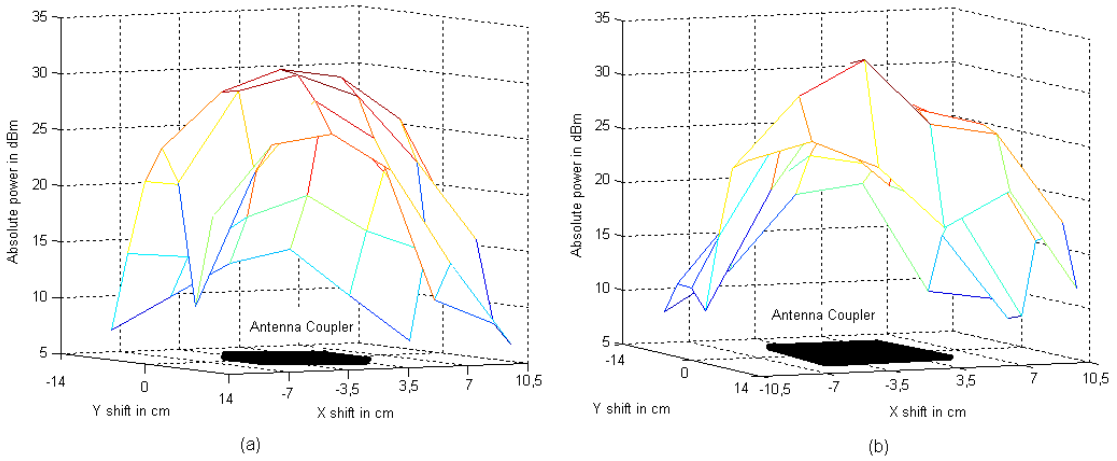

Figure 3.4: Power measurements at different positions of the RF shield box. (a) GSM 850 band (b) GSM 1900 band

Measurements from GSM 850 band seemed to exhibit a certain symmetry that was not seen in the GSM 1900 band. Although not an exhaustive approach, these coarse measurements served as a preliminary exploration for some possible locations where a sweet spot might be found: the power levels were the highest above the antenna coupler; thus, a lower coupling loss could be expected in that particular area. This and other criteria eventually guided my search as will be described in more detail at the end of this chapter, where a more reliable method is presented. A summary of the specifications of the antenna coupler is presented in Table 3.1.

Table 3.1: Electrical parameters of antenna coupler

Frequency range	800∼6000MHz
RF connector	SMA(Male)
Terminal impedance	50Ω
VSWR	≥1:2.2(Typ. 1.8)
Polarization	LHCP

Next, we present a description of the high performance coaxial cable used to connect the RF shield box to the radio communication tester, and also that of an accessory that allowed better accuracy in our measurements: a ferrite choke.

position.

3.1.3 High Performance Coaxial Cable

Transmission of RF energy from the antenna coupler to the radio communication tester and vice versa requires a transmission line capable of fulfilling a set of electrical and mechanical requirements needed to ensure the integrity of the signal transmitted, as well as the necessary enclosure to avoid unwanted radiation or interference. Coaxial cables are a widely popular preference in RF measurements. Depending on a given application, however, a conventional coaxial cable may underperform on a set of measurement conditions and become a significant source of uncertainty. Therefore, the selection of an appropriate coaxial cable is not a trivial matter. Given such constraints as the signal levels, phase and frequency stability, data integrity, repeatable nature of our measurements, among others, the connection of the RF shield box to the radio communication tester calls for the use of a high-quality coaxial cable. When talking about coaxial cables, one tacitly refers also to their concomitant companions, RF connectors, and thereby the stringent performance requirements apply to the whole set. A good starting point is to consider a cable with a low insertion loss and good impedance matching properties across the frequency range of interest [27, p. 199]. In choosing the most suitable cable, additional criteria have been considered following many of the recommendations outlined in [28, p. 67-78], [29], and [30]. These criteria are presented below.

- *Characteristic impedance:* The cable impedance has to match those of the antenna coupler and radio communication tester, that is, 50Ω, in order to avoid unwanted reflections. The characteristic impedance of a coaxial cable is given by the ratio of the diameter of the outer conductor to that of the inner conductor and the dielectric constant of the insulating material between the conductors.

- *Attenuation:* Attenuation is the loss undergone by the RF signal as it travels across the cable length. This attenuation mainly stems from conductive and dielectric losses, and it increases with frequency. Dielectric losses increase linearly with frequency, whereas conductive losses increase with the square root of frequency. Cable losses are inversely proportional to cable size, so larger cables experience lower losses. Two desirable qualities in regards to attenuation are the uniformity and stability. The former is understood as the feature by which the attenuation has a periodic response across the frequency range, and no narrow-band spikes occur. The latter refers to the endurance of the attenuation response, over time and flexure, to deleterious effects such as corrosion, moisture penetration or the ingress of other extraneous contaminants. Cables with silver plated braids present less degradation in their attenuation. Our eventual choice has a low, stable, and uniform attenuation response, with

a maximum value of around 0.5dB/m at frequencies above 2GHz.

- *Shielding effectiveness:* Just as it was the case with the RF shield box, a coaxial cable should be a conduit through which RF energy is transmitted so that the least amount of signal leakage is allowed, thus curtailing the interference affecting external electronic equipment. By reciprocity, it protects the RF signal from external sources of interference. The shielding efficiency of a coaxial cable relies on the structure of the outer conductor. Typical constructions include single braid, double braid, and triaxial configurations. Single braid consists of bare, tinned, or silver plated round copper wires, while double braids include two layers of the former, with no insulation between the layers. A triaxial configuration is the same as the double braid, with an insulation between the layers. A pair of braids with different patterns achieve an outstanding level of shielding, 90 to 100dB. This configuration is featured in our choice.

- *Capacitance:* Manufacturers often include capacitance as part of the distributed parameters by which the electrical properties of a coaxial cable can be characterized. Knowing the capacitance and the velocity of propagation, the distributed inductance is immediately derived. A lower capacitance creates a lower loading for data communications applications [28, p. 73]. In our measurements this is of great concern, for instance, when running Bit-error sensitivity search testings.

- *Velocity of propagation:* The velocity of propagation in a coaxial cable depends on the inverse of the square root of dielectric constant of the insulating material between the inner and outer conductor [2, p. 100]. Manufacturers express the velocity of propagation as a percentage of the velocity of light in free space. Our cable is stated to allow a 77% of the latter.

- *Cut-off Frequency:* In addition to the fundamental TEM mode, coaxial lines can support TE and TM waveguide modes [2, p. 127]. These higher order modes set an upper limit on the size of the coaxial cable and its maximum operating frequency, and in general it is desired to avoid the propagation of those modes. The cut-off frequency of a coaxial cable is determined by the dominant TE_{11} mode, and in our cable the cut-off frequency is set at 26.5GHz, exceedingly above our test frequencies.

Apart from the criteria described above, additional parameters that were considered in the selection of the coaxial cable were the power rating, the maximum operating voltage, and the operating temperature range. A summary of the features of the high-performance coaxial cable selected are shown below.

Element	Description
1. Center conductor	Stranded silver-plated copper wire
2. Dielectric	Low density Polytetrafluoroethylene PTFE
3. First outer conductor	Wrapped silver-plated copper tape
4. Second outer conductor	Silver-plated copper braid
5. Jacket	Polyurethane

A careful handling of RF connectors and coaxial cables is mandatory in order to avoid damage and/or measurement errors. Two fundamental practices are to keep the connectors clean and to apply the right torque when tightening the connectors. The latter should always be performed by turning the male connector, that is, by rotating the nut and keeping the inner conductor stationary. These and further recommendations [27, p. 200] were duly followed during the setup of our measurement system and the subsequent radiated measurements.

Ferrite choke

The high performance coaxial cable just described guaranteed a high level of accuracy in our measurements with regards to the signal path between the radio communication tester and the RF shield box. As mentioned in the beginning of Section 3.1, the antenna coupler is connected to the port of the RF shield box via a conventional thin coaxial cable. The reason for the selection of this type of cable is twofold and mainly answers dimensional needs, to wit: the cable has to be thin enough to fit a groove on the plate where the antenna coupler is embedded, and it should not be too long (about 20 cm). A conventional coaxial cable available in the lab facilities serves this purpose. This conventional cable, however, does not possess the high performance qualities described above, and being inherently smaller than the high performance cable, it offers a worse level of attenuation and the shielding effectiveness also decreases. Moreover, a more worrying phenomenon occurs on the coaxial cable inside the RF shield box. It was indicated above that a balun can be assumed to be incorporated in the antenna coupler to suppress unbalanced currents flowing on the surface of the outer conductor of the feeding coaxial cable connected to the spiral antenna. Thus, the currents flowing on the coaxial cable connecting the antenna coupler to the SMA connector mounted on the inside wall of the RF shield box are balanced out by the in-built balun. However, the currents flowing on the high-performance coaxial cable (connecting the RF shield box to the radio communication tester) cannot be balanced by the balun of the antenna coupler. These unbalanced currents are troublesome because they flow on the exterior surface of the outer conductor of the conventional coaxial cable (the one connecting the antenna coupler and the SMA connector on the wall of the RF shield box) and radiate inside the RF shield box, causing measurement errors. A common way to mitigate

such deleterious effect is to attach a series of snap-on ferrite choke beads along the troubled cable.

All materials can be classified into two main groups [31]: linearly and non-linearly magnetic. Materials such as ferromagnetic and ferrimagnetic belong to the latter and their main feature is that they exhibit a magnetic saturation once a given magnetic bias field is applied on them. Furthermore, given the particular chemical composition and crystal structures [4] that make a ferrimagnetic material such as ferrites, the material properties are said to be anisotropic. Recall that in section 2.1 we set out to conduct an analysis of Maxwell's equations assuming that the medium of propagation was isotropic, that is, a property that guaranteed the uniformity of the material regardless of the direction of the existing fields. Ferrites, on the contrary, are made of clusters of differently aligned magnetic dipoles called magnetic domains [31]. When a magnetic field is applied on the ferrite, the walls of the magnetic domains move and those domains pointing in the direction of the applied field grow in magnitude, while those pointing in other directions decrease. The magnetic bias field aligns the magnetic dipoles such that a net magnetic dipole is created prompting the magnetic dipoles to precess at a frequency that is proportional to the strength of the applied magnetic field [32, p. 35]. The precession movement is analogous to the movement a gyroscope undergoes when subjected to a gravitational field. There exists, then, a coupling between the precession of a ferrite magnetic dipole and the magnetic field applied. This coupling is called gyroscopic coupling [31]. An interesting phenomenon occurs when the frequency of the applied magnetic field equals that of the precession, giving rise to a *gyromagnetic resonance* or *ferrimagnetic resonance*. Under resonance conditions, the permeability of the ferrite becomes a complex factor derived from a tensor susceptibility matrix [2, p. 446]

$$[\chi] = \begin{bmatrix} \chi_{xx} & \chi_{xy} & 0 \\ \chi_{yx} & \chi_{yy} & 0 \\ 0 & 0 & 0 \end{bmatrix}$$

where the matrix elements are given as

$$\chi_{xx} = \chi_{yy} = \frac{\omega_0 \omega_m}{\omega_0^2 - \omega^2} \qquad \chi_{xy} = -\chi_{yx} = \frac{j\omega\omega_m}{\omega_0^2 - \omega^2}$$

The frequencies ω_0 and ω_m depend on the applied magnetic bias field and the magnetization vector, respectively. Intuitively, χ_{xx} and χ_{xy} are identified as the real and imaginary parts of the complex susceptibility. When the frequency of the RF field, ω, equals ω_0 a gyromagnetic resonance occurs, leading to a singularity analo-

[4] A more detailed description of the crystalline structures and an in-depth analysis at the atomic level following a quantum mechanics approach is offered in [32].

gously encountered in a resonant LC circuit. Such singularity would go unbounded, but in reality is damped out by a linewidth factor or loss factor similar to the Q factor in the said circuit. This loss is different from the dielectric loss that a ferrimagnetic material may have [2, p. 451]. There exists also a *demagnetization factor* that relates the internal and external RF fields of the ferrite, and which depends on the shape of the ferrite and the orientation of the fields. This demagnetization factor directly affects the gyromagnetic resonance frequency.
The foregoing discussion has highlighted some of the intricate phenomena proper to ferrites and in passing, this has led to the introduction of a loss factor linked to the gyromagnetic resonance frequency. Let us recall that our intent is aimed at explaining the rationale behind the use of ferrites in our measurement system as a means of suppressing unwanted fields present on the coaxial cable inside the RF shield box. This rationale is necessarily predicated on the resistive losses responsible for the attenuation of deleterious interference. In broader terms, any attenuation is attained by subjecting a current or field to traverse a resistive or high impedance element. A ferrite provides one such high impedance path as is explained below. Snap-on ferrites are easily attached on interfering-current-carrying coaxial cables as illustrated in Figure3.5.

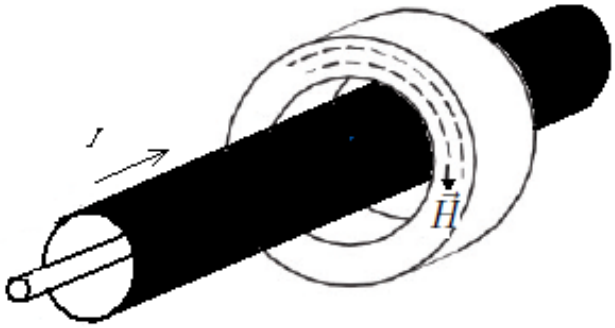

Figure 3.5: Snap-on ferrite choke attached on coaxial cable to mitigate interfering fields $\vec{H}$ stemming from unbalanced current flowing on the surface of the outer conductor of the cable.

As the frequency nears that of the ferrimagnetic resonance, the ferrite impedance becomes more resistive and the ferrite becomes lossy causing the disruptive RF fields to be dissipated in the bulk of the material. Even at higher frequencies, above the ferrimagnetic resonance frequency, the ferrite effectively attenuates such fields. Typical ferrite impedance values do not exceed the 300Ω-margin, and attenuation values to be expected range from 6 to 10dB; even 20dB can be attained at certain frequencies where the cable has a low impedance [33].

This section concludes our analysis of the fundamental components of the measurement system. Next, we present a description on how the sweet spots were

obtained and the criteria followed for their selection.

3.2 Sweet Spots in Radiated RF Measurements

Our discussion so far has presented the measurement system in its details. Once the measurement system is set up, the next step is aimed at determining the most suitable position inside the RF shield box, where the phone under test is placed so that measurements are reliable and accurate. At present, 4G phones are designed to serve different cellular bands ranging from 700 up to 2500MHz and this is achieved by a complex accommodation of various antenna structures inside the phone handset. A certain band may present a given radiation pattern, while that of other band is completely different and the corresponding radiation center of the phone may vary. Moreover due to the dimensions of the RF shield box, our measurements are conducted in the near-field region where the interaction of the electromagnetic fields between the antenna coupler and the phone antennas poses a significant challenge to find the most suitable location of the phone. It was indicated in sub-section 2.2.2 that the near-field region is divided in a reactive and radiating sub-regions. In the former the predominant fields are reactive and the antenna pattern is poorly defined with no clear outline of the main and secondary lobes. In the radiating near-field region, the angular field distribution depends on the distance from the antenna [34] and lobes begin to form an incipient pattern that resembles the one characteristic of the actual far-field region. The sweet spot location must necessarily provide a viable compromise in terms of the level of coupling loss and attenuation uniformity across the different bands being tested in both near-field sub-regions.

With this background in mind, I decided that the most important criteria to find an appropriate sweet spot would need to include three fundamental guidelines, to wit:

1. The attenuation response observed should be as flat as possible across the bands to be tested.

2. The attenuation should be as low as possible so that the coupling loss is minimized.

3. Finally, it should be highly desirable to obtain a single sweet spot where each and every band can be tested and the former criteria are met.

As it will be shown later, the last criterion turned out to be a very challenging endeavor, and although one unique sweet spot worked well for the vast majority of parameters across all bands of interest, an alternative sweet spot had to be used for a particular parameter. Likewise, the low coupling loss restriction may be safely relaxed since such losses can be compensated for by adding the appropriate path loss

values in the radio communication tester. Our first approach to finding the sweet spot following the criteria just described was to conduct the measurements with a sample phone on a trial-and-error basis for each frequency band. Naturally, this heuristic approach worked well but it was very time consuming. Manual measurements were conducted on an active phone and the parameters evaluated were the nominal output power and the sensitivity level. Each band of interest was tested on its low, mid and high channels. The appropriate settings following the corresponding specifications, as it will be described in the next chapter, were set in the radio communication tester and the power and sensitivity were measured. The attenuation values were then read from the instrument as the power and sensitivity levels were adjusted to fit nominal requirements. A rough estimate could also be deduced from the power measurements, shown in Figure 3.4, concerning possible locations where the power readings were the highest and the power distribution was rather flat. Nevertheless, my efforts were reduced to try many positions, run the measurements, and note down the attenuation values.
Fortunately, a more efficient method was possible thanks to the use of a phone assembly designed to conduct standalone tests on the phone antennas. The assembly enabled me to measure the S21 parameter with a VNA in a setup like the one illustrated in Figure 3.6. Such assembly consisted of the whole set of mechanics as any of the regular smart phones subsequently tested, but with no active phone calls enabled. A small SMA pigtail coaxial cable was soldered on the port of the main antenna of the phone. This allowed the connection of two additional coaxial cables down to one of the VNA ports.

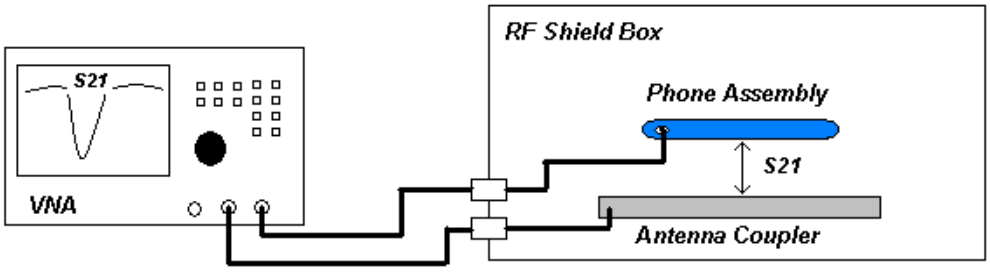

Figure 3.6: Diagram of setup used to measure S21 parameters between phone assembly and antenna coupler.

An evaluation of the S21 parameter does not represent the complete path loss because the reference ports have been shifted while calibrating the VNA to the end of the coaxial cables inside the RF shield box. This setup, however, accounts for the larger amount of attenuation since the losses due to the cables and connectors are very small if compared to the coupling loss incurred by the separation between the phone and the antenna coupler. Under this new setup possible sweet spots

are identified more readily as the attenuation response displayed in the VNA is gauged against the first two criteria described above, namely the least attenuation and flattest response. Figure 3.7 shows the S21 parameter measured when the

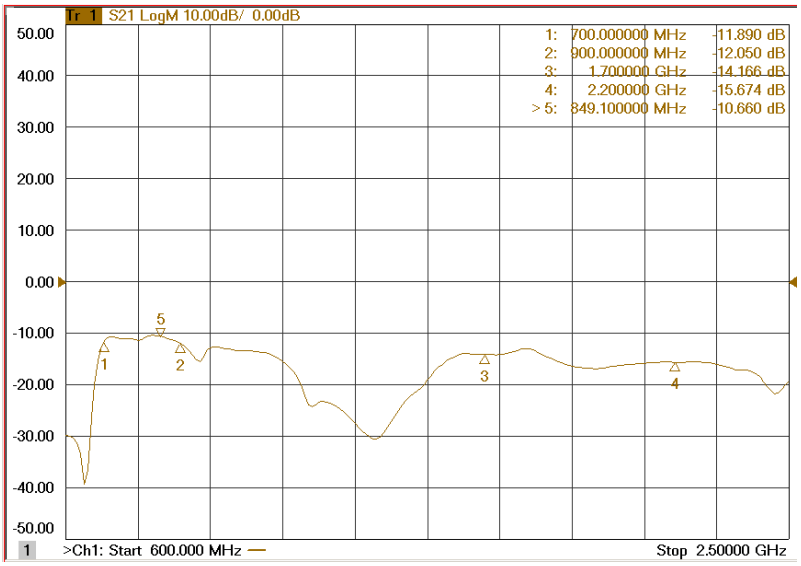

Figure 3.7: S21 measured when phone was placed at 0.8cm from antenna coupler. A single layer of RF absorber is placed at the bottom of the RF shield box. The ordinate shows the magnitude of the S21 parameter in [dB] and the frequency range set on the VNA is shown on the abscissa. Markers have been included to showcase frequencies of interest in our tests.

gap between the phone and the antenna coupler was 0.8cm. Markers indicate the demarcation where the response is flat across the frequency bands of interest. In the next chapter these frequencies will be stated in detail, but for the present discussion it will suffice to broadly define the frequency ranges of interest from 700 to 900MHz, and from 1800 to 2200MHz. In a similar fashion, the S21 parameter was measured by positioning the phone 6cm away from the antenna coupler. Figure 3.8 shows the said parameter with the 6cm gap.

As expected, the distance increase translates into an increment of the coupling loss, 10dB in this case. The flatness, however, remains considerably unaltered as shown. It should be noted that the S21 measurements served in turn to test the number of the layers of carbonyl iron loaded urethane rubber absorbers to be placed at the bottom of the RF shield box. Figures 3.7 and 3.8 show the S21 measurements when a single layer of RF absorber was added at the bottom of the RF shield box. The same measurements were conducted with two layers of RF absorbers. Measurements obtained from the reactive near-field sub-region were basically the same in both cases, while a slight variation was observed in those conducted in the reactive near-field sub-region. Figure 3.9 shows this difference.

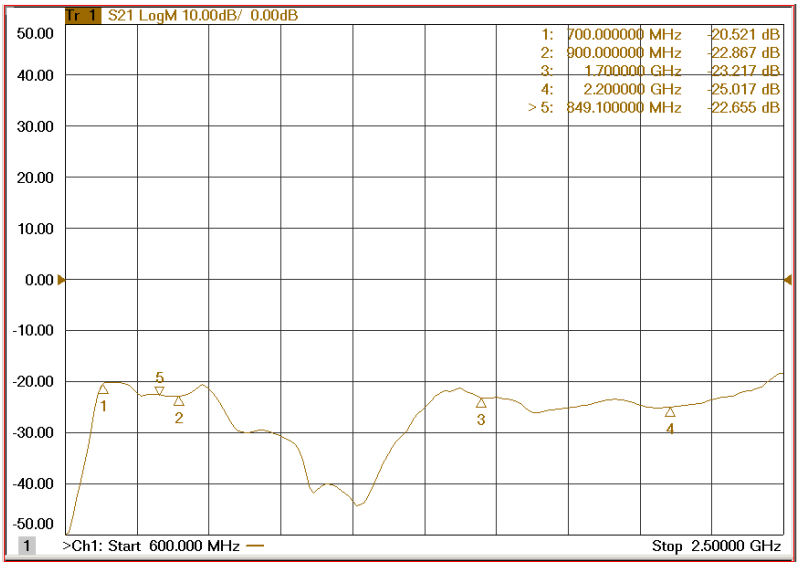

Figure 3.8: S21 measured when phone was placed at 6cm from antenna coupler. A single layer of RF absorber is placed at the bottom of the RF shield box. The ordinate shows the magnitude of the S21 parameter in [dB] and the frequency range set on the VNA is shown on the abscissa. Note that the magnitude of S21 has doubled by increasing the testing distance.

S21 measurement results indicated then, that neither the level of coupling loss nor the attenuation flatness was substantially affected by using only one or two layers. Nevertheless, subsequent testing of the proper parameters of the phone, as explained in the next chapter, showed that the overall capability performance (better Cpk values) of the output power and sensitivity in some bands was slightly improved by the inclusion of only one single absorber. A possible reason for this, as it was suggested by a colleague at the company, is the variation of the thickness between the upper wall and the bottom (including the RF absorbers) of the RF shield box. By including more absorber layers at the bottom, the thickness [5] becomes more comparable to the wavelength of the fields confined in the RF shield box, giving rise to more losses. Although a feasible hypothesis, it demands further study and measurements. In chapter 4, I will only include the measurement results obtained when a single layer of RF absorber was used.

It is important to note that once an appropriate sweet spot has been found, it is fundamental to ensure a good repeatability [6] of the measurements by holding every phone at exactly the same position. For that purpose, the use of Styrofoam and a jig will be indicated in the next chapter.

This section concludes our analysis of the measurement system. The following chap-

[5] The original height inside the RF shield box is 17cm. The thickness of the RF absorber layer is 0.5cm, so two layers reduce the height of the RF shield box to 16cm.

[6] Repeatability is a measure of the consistency of the same measurement performed by the same operator [16].

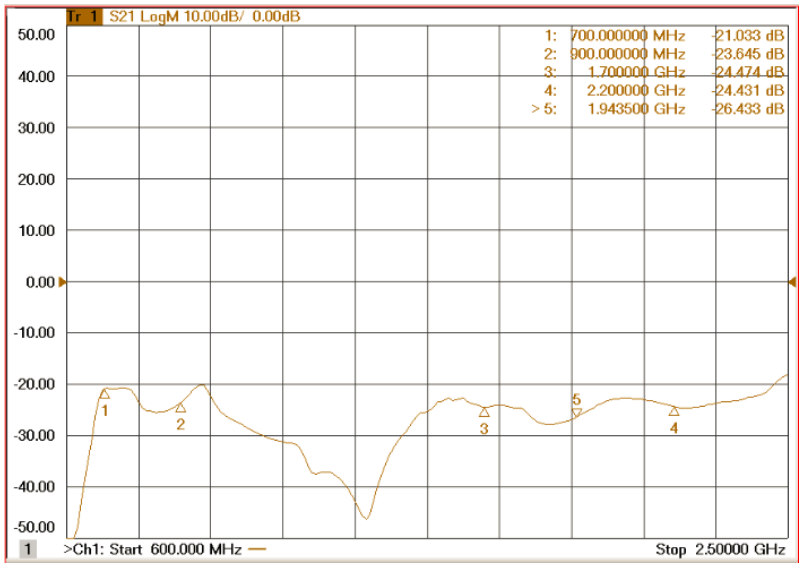

Figure 3.9: S21 measured when phone was placed at 6cm from antenna coupler. Two layers of RF absorbers are placed at the bottom of the RF shield box. The ordinate shows the magnitude of the S21 parameter in [dB] and the frequency range set on the VNA is shown on the abscissa.

ter presents an account of how the performance parameters of the phone were measured and the corresponding discussion of the results obtained.

4. RADIATED RF MEASUREMENTS AND DISCUSSION OF RESULTS

The foregoing chapters described the physical phenomena underlying the radiated measurements under consideration in this thesis as well as the hardware components of the measurement system. Chapter 2 presented the theoretical background on the electromagnetic fields that form the basis of the phenomena being evaluated. It also introduced the reader to some basic principles of statistics and process capability analysis needed for the proper comprehension of the results that will be presented in a later section of the current chapter. Chapter 3, in turn, described in detail the system setup used for the measurements and gave an insight into the concept of sweet spot for conducting the radiated measurements.
The present chapter is intended to expound on the actual radiated measurements and the subsequent statistical analysis derived from their results. At first, we present a description of the test settings employed in the measurements. This includes a summary of the settings specified by the 3GPP conformance testing standard, as well as an account of the specific parameters evaluated in our measurements. An ensuing section explains how the attenuation values are obtained to account for the entire path loss. These values were then input into the radio communication tester in order to compensate for the path losses and thus calibrate the system. Section 4.3 offers an analysis of the process capability results yielded by the RF measurements. As it was indicated in Section 2.3.2, the main benchmark that is used to assess the compliance of the process capability to the industry standards is a Cpk of 1.5, as mandated by a quality control method known as Six Sigma. Finally, subsection 4.3.3 presents a brief discussion on the overall level of uncertainty to be expected in the measurement results.

4.1 Tests Settings and Specifications

We begin our discussion by reviewing the specifications and recommendations that our measurements must comply with as dictated by the standardization body, 3GPP. The 3rd Generation Partnership Project (3GPP) is a regulatory entity that unites telecommunications standard development organizations (and provides an environment conducive to produce the reports and specifications that define 3GPP technologies). 3GPP comprises four Technical Specification Groups (TSG): Radio Access

Networks (RAN), Service & System Aspects (SA), Core Networks & Terminals (CT) and GSM EDGE Radio Access Networks (GERAN). Each of the four TSGs has a particular area of responsibility for the reports and specifications that belong to its own terms of reference [35]. Each TSG has a set of Working Groups (WG). The RF radiated measurements considered in this thesis fall into the technical specification group RAN (TSG RAN) specifically, under the working group RAN WG5. TSG RAN is responsible for the definition of the functions, requirements and interfaces of the UTRA/E-UTRA network in its FDD and TDD modes. Our interest is focused on the radio performance and mobile terminal conformance testing.

The following sub-sections summarize the test settings and specifications followed in our measurements. As a reminder, the specifications presented encompass all the parameters required to be tested according to 3GPP. However, for the sake of brevity only the transmitter output power and receiver sensitivity parameters are analyzed in depth. These parameters are chosen due to their relevance to the performance of both the mobile handset and the cellular network. Moreover, only the results of selected bands will be presented in a later section as they are representative samples of the wide range of frequencies in the different mobile technologies tested herein.

4.1.1 GSM Specifications

Table 4.1 summarizes all the measurement parameters evaluated in GSM and some of their most important settings; the frequency ranges covered by the different GSM bands tested are shown in Table 4.2.

Table 4.1: GSM RF Radiated Measurement Parameters as specified by 3GPP[36] and [37].

Measurement Parameters	***Band***	***Channel***	***PCL***	***Sample Size***	***Lower Limit***	***Upper Limit***	***Units***
TX Power	GSM850/900	Low, Middle, High	5	100 bursts	30	36	dBm
RMS Phase Error	GSM850/900	L,M,H	5	100 bursts	-5	5	°
Peak Phase Error	GSM850/900	L,M,H	5	100 bursts	-20	20	°
Frequency Error	GSM850/900	L,M,H	5	100 bursts	-0.1	0.1	ppm
BER Sensitivity Search	GSM850/900	L,M,H	5	100 frames		-102	dBm
TX Power	DCS1800 PCS1900	L,M,H	0	100 bursts	27	33	dBm

continued on next page

continued from previous page

Measurement Parameters	***Band***	***Channel***	***PCL***	***Sample Size***	***Lower Limit***	***Upper Limit***	***Units***
RMS Phase Error	DCS1800 PCS1900	L,M,H	0	100 bursts	-5	5	°
Peak Phase Error	DCS1800 PCS1900	L,M,H	0	100 bursts	-20	20	°
Frequency Error	DCS1800 PCS1900	L,M,H	0	100 bursts	-0.1	0.1	ppm
BER Sensitivity Search	DCS1800 PCS1900	L,M,H	0	100 frames		-102	dBm

Table 4.2: GSM frequencies as specified by 3GPP [37].

GSM band	***Uplink frequencies (MHz)***	***Downlink frequencies (MHz)***
GSM 850	824 - 849	869 - 894
GSM 900	890 - 915	935 - 960
DCS 1800	1710 - 1785	1805 - 1880
PCS 1900	1850 - 1910	1930 - 1990

The transmitter (Tx) output power is the averaged power radiated by the mobile station over the time when the useful bits of the burst are transmitted [36]. The power control levels must set the nominal output power level to maximum according to the power class to which the mobile station belongs. A normal tolerance margin of ±3dB has been applied as indicated by the limits shown [36, p. 196-197].

The frequency error is defined as the difference in frequency, once the effect of modulation and phase error have been adjusted, between the RF signal transmitted from the mobile station and the base station. The phase error, on the other hand, is the difference in phase, after the effect of the frequency error has been adjusted, between the RF signal transmitted from the mobile station and the theoretical transmission as given by the intended modulation [36]. 3GPP standard [36, p. 179] recommends the following conformance requirements, applicable to both GSM850 and PCS1900: The MS carrier frequency should be accurate to within 0.1 ppm; the RMS phase error, defined as the difference between the phase error trajectory and its linear regression on the active part of the time slot, should not exceed 5° for any burst, whereas the maximum peak deviation should be lower than 20°, as indicated in Table 4.1. Finally, the receiver sensitivity is the lowest RF power received at the antenna port, which can generate a useful signal that complies with a predefined signal-to-noise ratio. The reference sensitivity is quantified in terms of bit error rate BER. The bit error rate is the ratio of the bits wrongly received to all data

bits transmitted. In our measurements, we have set the BER at 2.4%. The actual sensitivity level of the phone should be lower than the specified limit known as the reference sensitivity level, shown in Table 4.1. These reference sensitivity levels are specified in [37, p. 34].

4.1.2 WCDMA Specifications

As mentioned above the TX output power and reference sensitivity are also evaluated in WCDMA. These and the other parameters tested are shown in Table 4.3. The operating frequencies for the bands tested are shown in Table 4.4.

Table 4.3: WCDMA RF Radiated Measurement Parameters as specified by 3GPP [38].

Measurement Parameters	***Band***	***Channel***	***Sample Size***	***Lower Limit***	***Upper Limit***	***Units***
Maximum Output Power	I, II	L,M,H [1]	50	21	25	dBm
Error Vector Magnitude	I, II	L,M,H	50		17.5	%
Frequency Error	I, II	L,M,H	50	-0.1	0.1	ppm
BER Sensitivity Search	I	L,M,H	200		-106	dBm
	II				-104	dBm
Maximum Output Power	V, VIII	L,M,H	50	21	25	dBm
Error Vector Magnitude	V, VIII	L,M,H	50		17.5	%
Frequency Error	V, VIII	L,M,H	50	-0.1	0.1	ppm
BER Sensitivity Search	V	L,M,H	200		-104	dBm
	VIII				-103	dBm

Table 4.4: WCDMA frequencies as specified by 3GPP [38].

WCDMA band	***Uplink frequencies (MHz)***	***Downlink frequencies (MHz)***
I	1920 - 1980	2110 - 2170
II	1850 - 1910	1930 - 1990
V	824 - 849	869 - 894
VIII	880 - 915	925 - 960

The nominal maximum output powers and their corresponding tolerances are determined according to the power class of the UE. The maximum output power is defined as a measure of the maximum power the UE can transmit within a bandwidth larger than $(1+\alpha)$ times the radio access chip rate [38], where α is the roll-off factor of the root-raised cosine filter. A root-raised cosine filter with a roll-off α=0.22 increases the WCDMA signal bandwidth by 22% so that the original bandwidth of 3.84MHz becomes approximately 4.6MHz [**?**, p. 182].

[1] Low, Middle, and High.

An appropriate power level is crucial since a level too high may cause interference with other channels or systems, and a level too low decreases the coverage area. The limits shown in Table 4.3 correspond to a Power Class 3 UE whose output power is set at 24dBm and the tolerance is +1/-3 dB, as specified in [38, p. 64]. A parameter tested in WCDMA and LTE but not in GSM, is the error vector magnitude EVM. EVM is a metric that measures the modulation quality, and it is defined as the difference between a reference waveform and the measured waveform [39, p. 108]. A graphical representation aids in understanding this difference. Figure 4.1 shows the EVM of a QPSK signal. The vectors portrayed are the ideal signal vector V_{ref}, the actual received signal vector V_{meas} and the error vector V_{error} that results from their difference. The axes are the in-phase I and quadrature Q components of the constellation diagram of a QPSK signal. Both waveforms (reference and measured)

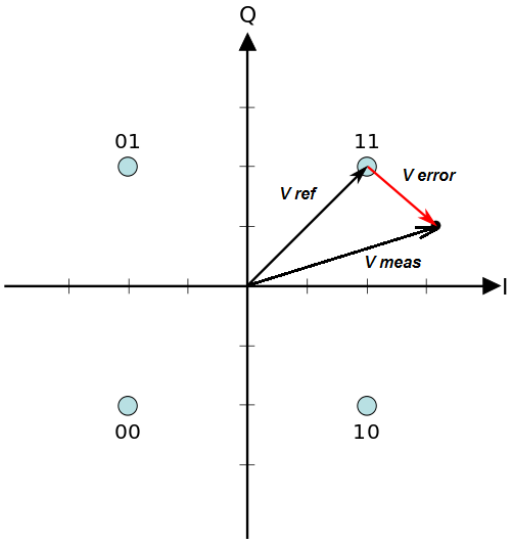

Figure 4.1: EVM of QPSK signal. Figure edited from Wikipedia.

pass through a matched root-raised cosine filter. The EVM value is given as the square root of the ratio of the mean error vector power to the mean reference power expressed as a percentage. 3GPP standard specifies [38, p. 197] that the EVM should not exceed 17.5%. This range tolerance is identified by the area confined by the circle traced by the error vector V_{error} shown in 4.1.

The frequency error bears a similar definition as that stated for GSM. [38] defines it as the difference between the RF modulated carrier frequency that the UE transmits and the assigned frequency from the base station. The UE receiver's generated RF signal must be synchronized to the RF signal received from the base station. Due to the latter's own frequency error and Doppler shifts [1] the said signals will

[1] Common to all wave phenomena, the Doppler frequency shift is the difference between the frequency of the received wave and that of the transmitted wave due to the relative motion between the transmitter and the receiver [11].

have an apparent error. It should be noted that because we are interested in testing the UE transmitter, and the Doppler shifts pertain to the properties of the mobile radio channel, signals from the base station should be averaged over sufficient time so that errors derived from the radio channel characterization are accounted for in the minimum requirements specified by 3GPP standard, which sets the acceptable limits for this error to ±0.1ppm [38, p. 95].

The receiver characteristics are evaluated by different tests: the reference sensitivity measurement, maximum input level, selectivity and intermodulation measurements, among others. We have evaluated only the reference sensitivity, by way of the BER as specified by 3GPP which states that the BER should not exceed 0.1% [38, p. 235]. The minimum sensitivity level that the receiver should be able to detect is set at -104dBm, for both band II and V, -106dBm for band I, and -103dBm for band VIII. A deficient reception sensitivity reduces the coverage area at the far end from base station.

Further settings used in our measurements are found in section E.3.1 and E.3.2 from Appendix E in [38].

4.1.3 LTE Specifications

Table 4.5 shows the settings and parameters followed in LTE measurements. The operating LTE frequencies for the bands tested are described in Table 4.6.

Table 4.5: LTE RF Radiated Measurement Parameters as specified by 3GPP [40].

Measurement Parameters	***Band***	***Channel***	***RB Size***	***Sample Size***	***Lower Limit***	***Upper Limit***	***Units***
Maximum Output Power	3, 4	L,M,H [1]	50	20 slots	21	25	dBm
Error Vector Magnitude	3, 4	L,M,H	50	20 slots		17.5	%
Carrier Leakage	3, 4	L,M,H	50	20 slots		-25	dBc
Frequency Error	3, 4	L,M,H	50	20 slots	-0.1	0.1	ppm
ACLR	3, 4	L,M,H	50	20 slots	30		dB
Reference Sensitivity	3	L,M,H	50	20 slots		-94	dBm
level	4					-97	dBm
Maximum Output Power	17, 20	L,M,H	50	20 slots	21	25	dBm
Error Vector Magnitude	17, 20	L,M,H	50	20 slots		17.5	%
Carrier Leakage	17, 20	L,M,H	50	20 slots		-25	dBc
Frequency Error	17, 20	L,M,H	50	20 slots	-0.1	0.1	ppm

continued on next page

continued from previous page

Measurement Parameters	***Band***	***Channel***	***RB Size***	***Sample Size***	***Lower Limit***	***Upper Limit***	***Units***
ACLR	17, 20	L,M,H	50	20 slots	30		dB
Reference Sensitivity level	17, 20	L,M,H	50	20 slots		-94	dBm

Table 4.6: LTE frequencies as specified by 3GPP [40].

LTE band	***Uplink frequencies (MHz)***	***Downlink frequencies (MHz)***
3	1710 - 1785	1805 - 1880
4	1710 - 1755	2110 - 2155
17	704 - 716	734 - 746
20	832 - 862	791 - 821

All the measurements were made for a QPSK modulation scheme, a 10MHz channel bandwidth, and an FDD mode. The maximum output power is defined as the mean power in the channel bandwidth measured over at least one subframe (1ms) [39, p. 105]. In the same fashion as in WCDMA, an excessive power level may interfere to other channels or systems, while a scarce level reduces the coverage area. An efficient power amplifier design aids in conserving battery power in the UE. Nonetheless, in an LTE technology the phone has to transmit LTE signals with different configurations of channel bandwidth, resource block allocation and modulation scheme, so that in some uplink transmission scenarios (especially with large resource blocks allocations) the amplifier may operate in the non-linear region [39]. Output power is indeed very crucial in LTE and its level is chosen once again according to the UE power class. For a power-class 3 UE, 3GPP standard dictates a maximum power output of 23dBm, and a tolerance of $\pm$2dB [40, p. 53]. The error vector magnitude bears the same definition presented in the previous WCDMA parameters. In LTE, the EVM is evaluated for the Physical Uplink Shared Channel PUSCH, the uplink demodulation reference signal, the Physical Uplink Control Channel PUCCH and the Physical Random Access Channel PRACH preamble. 3GPP standard [40, p. 297]specifies that the PUSCH EVM (and that for the demodulation reference signal) should be lower than 17.5% for QPSK. EVM can be defined with respect the frequency domain or the time domain. In our measurements it is the latter the domain chosen, and the EVM is measured with respect to a set of timeslots or subframes. The radio communications tester used for the measurements allows the evaluation of a low and a high EVM. These depend on the timing selected for the EVM measurement. Another metric used to quantify the modulation quality is the

[1]Low, Middle, and High.

carrier leakage or IQ (origin) offset. The 3GPP standard defines the carrier leakage as an interference caused by local oscillator (LO) leakage and it manifests itself as an unmodulated sine wave at the carrier frequency. This wave causes interference especially to the center subcarriers in the UL [40, p. 304]. 3GPP sets the minimum requirement for the relative carrier leakage power at -25dBc when the phone's output power is greater than 0dBm [40, p. 304]. The minimum requirement for the frequency error is again confined by the limits ±0.1ppm, [40, p. 290].

Further parametric measurements in LTE include the output RF spectrum emissions. These comprise occupied bandwidth, spectrum emission mask, or adjacent channel leakage power ratio ACLR, among others. We evaluated only the latter in our measurements. ACLR is a metric that is used to verify that the UE transmitter is not a source of unacceptable interference to adjacent channels. 3GPP distinguishes the adjacent bands whether they belong to UTRA or E-UTRA. ACLR is performed for one adjacent E-UTRA band, E-UTRA$_{ACLR1}$, and for two UTRA bands, UTRA$_{ACLR1}$ and UTRA$_{ACLR2}$. The ACLR is calculated as the ratio of the filtered mean power on the LTE channel to the filtered mean power on an adjacent channel frequency [39, p. 116]. The minimum conformance requirement for the E-UTRA$_{ACLR1}$ is specified as 30dB for a 10MHz channel bandwidth. As for the UTRA$_{ACLR1}$ and UTRA$_{ACLR2}$ the minimum requirements are 33dBc and 36dBc, respectively. These requirements are found in [40, p. 380-381].

The receiver characteristics in LTE are tested by measuring the reference sensitivity level, the maximum input level, the spurious emissions, among others. As in WCDMA, the reference sensitivity level is chosen to characterize the receiver quality. This test is performed by having a fixed downlink reference channel with a very low power level. The minimum levels specified by 3GPP for this fixed reference channel power level are -94dBm for LTE band 3, -97dBm for band 4, -94dBm for band 17 and band 20. The minimum conformance requirement in this test establishes that at the latter prescribed power levels, the receiver should be able to achieve a throughput greater or equal than 95% of the maximum throughput of the reference measurement channels [40, p. 497-498]. This maximum throughput is used by all the receiver tests (except for spurious emissions) as a compliance criterion, and for a QSPK-10MHz-FDD reference channel is specified by 3GPP as 3952.8kbps, averaged over one frame [40, p. 1089]. In a similar way as in WCDMA, an UE that fails to conform to the throughput requirement will reduce the coverage area of the base station.

The next section describes how the attenuation values that are to be compensated by the radio communication tester are obtained for both the input and the output paths.

4.2 Path Loss Measurement and System Calibration

Before any measurement can be made, it is necessary to conduct a correction of the losses incurred by the RF signals as they travel from the phone under test and the radio communication tester, and vice versa. This systematic correction begins by measuring the attenuation values in the RF path (both for Uplink (UL) and Downlink (DL)), and then by inputting those values into the radio communication tester, which automatically compensates for such losses once measurements are made. Thus, the system is calibrated.

A fully functional phone, often referred to as golden phone, is used for the measurements. This phone is tuned to accurate power levels so that all testing equipment can be calibrated with the same power levels and measurement errors from different test systems can be safely discarded. The phone will be placed in the sweet spots studied in Chapter 3, both at 0.8cm and 6 cm from the antenna coupler. The procedure follows the path loss measurement described in [41].

4.2.1 Uplink Path Loss

When an *external input attenuation* (see Figure 4.2) is entered into the radio communication tester, every power reading from the phone tested is increased to compensate for the losses undergone by the signal. Thus, the power reading displayed in the radio communication tester corresponds to the actual power level transmitted by the phone. Figure 4.2 illustrates the setup used to measure the path loss in the Uplink.

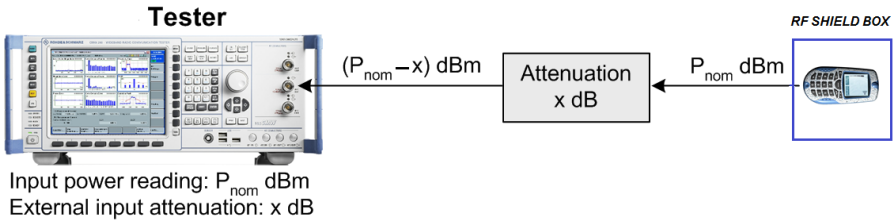

Figure 4.2: Definition of Uplink path loss. Edited from [41].

The path loss is calculated by measuring the power transmitted by the phone when a call is active. The goal is to read the power levels dictated by the 3GPP standards (referred to above) in the radio communication tester. Every technology (GSM, WCDMA, and LTE) is measured in its low, mid and high channels. Because of the path loss, the external input attenuation value has to be increased in the tester until the desired power levels are reached. Without entering any attenuation value to the radio communication tester, the power level read by the tester, $(P_{nom} - x)$, is lower than the actual output power transmitted by the phone, P_{nom}, due to the

losses. By entering the appropriate attenuation value into the tester, the actual power given by the phone is displayed in the tester.

4.2.2 Downlink Path Loss

In a similar manner, when an *external output attenuation* (see Figure 4.3) is reported to the radio communication tester the RF generator will increase its power level so that the nominal power received by the phone under test is devoid of the downlink attenuation as illustrated in Figure 4.3.

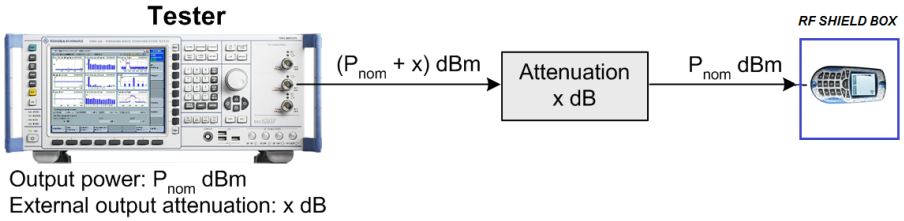

Figure 4.3: Definition of Downlink path loss. Edited from [41].

Analogous to the Uplink, the path loss in the downlink is calculated by varying an external output attenuation. In this case, however, we measure the reference sensitivity on the golden phone until the sensitivity levels specified by 3GPP are measured in the test instrument. Once again, we measure all technologies on their low, mid and high channels.

Once all the attenuation values were calculated for the UL and DL paths in all technologies, they were inputted into the software used to drive the radio communication testers so as to make the measurements in an automated manner.

4.3 Radiated RF Measurements and Discussion of Results

The Cpk values presented in this section will illustrate the RF parametric compliance of the 4G phones tested, to the stringent specifications prescribed by the 3GPP standard. They will also evince the fact that by choosing an appropriate sweet spot, RF radiated measurements can be conducted with the phone placed either in close proximity to the antenna coupler (0,8cm - reactive near-field sub-region), or at a distance away from the coupler (6cm) where at the tested frequencies the fields are sensed in the radiating near-field sub-region. The RF parameters of the tested 4G phone handsets conform to 3GPP specifications in both cases yielding very good Cpk values, indicative of a capable process.

As stated before, the parameters chosen to illustrate the above are the maximum TX output power and the RX sensitivity levels. A selected set of graphical representations of these parameters in the mid channels [2] are presented for both

[2] Cpk values were very uniform across all low, middle and high channels. We chose to show only

measurements conducted from the two distances mentioned above. Cpk values of all other parameters will also be shown for discussion. The software used to produce the statistical data and generate the capability graphs is Minitab®16. We first present the results obtained at 0.8cm from antenna coupler and then those yielded by the phone placed at 6cm from the coupler. In both cases, a piece of Styrofoam was used to hold the phones in place at the tested distances [3]. It is worth reiterating at this point the importance of having a good repeatability in our measurements by ensuring every phone is placed at exactly the same position. Styrofoam is a material commonly used in setups of radiated measurements not only because of its mechanical properties (easy to make structures for different testing purposes), but also due to its electromagnetic properties. For instance some of the properties of Styrofoam (103.7) at 3GHz [2, p. 687], are a dielectric constant of 1.03, and a loss tangent[4] of 0.0001. The values of these parameters for air are 1 and 0, respectively. Thus, the electromagnetic disturbance of Styrofoam in the field measurements is negligible and we can assume that it will not affect the accuracy of our results.

4.3.1 RF parametric evaluation and Cpk analysis when phone is at 0.8cm from antenna coupler (reactive near-field sub-region)

The results presented in this section validate the radiated RF measurements in the reactive near-field sub-region. The near-field sub-regions and far-field region were identified in Section 2.2.2. Figure 2.3 illustrated the regions for both electrically small and large antennas. Our focus in this thesis evidently is on electrically small antennas, and as it was portrayed in the same Figure for such antennas the radii delimiting the reactive near-field and the radiating near-field are estimated [6] as $R_1 = 0.16\lambda$ and $R_2 = 5\lambda$, respectively. A survey across the frequency bands tested in our measurements (as presented in Sections 4.1.1, 4.1.2, and 4.1.3) reveals the following: the limiting radius enclosing the reactive near-field is dictated by the highest frequency band, that is WCDMA I which in the DL spans from 2110 to 2170MHz. Taking the highest frequency, 2170MHz, the radius is calculated as 2.2cm. Thus, by making the measurements with the phone placed at 0.8cm from the antenna coupler, we ensure that they are conducted in the reactive near-field sub-region for each and every frequency band. Figure 4.4 shows the process capability of the output power of the phone for GSM850, CH 190.

Note that as it was clarified at the end of Section 2.3.2, even though the graphs generated by Minitab show the performance parameters Pp and Ppk, in effect they

the results obtained in the middle channel.

[3] However, a jig was eventually made to place the phones at 0.8cm.

[4] the loss tangent is a measure of the power loss in a medium [4].

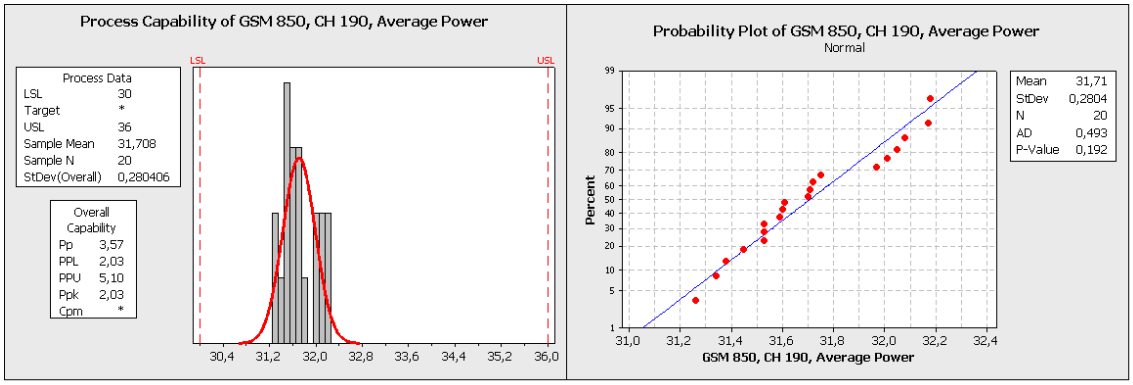

Figure 4.4: Process capability and Probability plot of output power in GSM 850

represent the process capability indices Cp and Cpk. Therefore, Pp and Ppk are shown and not Cp and Cpk in the plots. Furthermore, for our study only Ppk is considered. Additional data shown in the plots are the upper and lower specification limits (USL and LSL), sample mean, number of samples N, and the standard deviation. As for AD and $P-value$, they are irrelevant quantities for our study as it was explained in Figure 2.6. Figure 4.4 indicates that the process is very capable of meeting the specifications as attested by the high capability indices. Likewise, a normal distribution is verified by the probability plot.

It was indicated in Chapter 2 that a first step to verify our choice of 20 samples is reasonable for our statistical analysis, was to ensure the process was in control when both 20 and 150 samples were used. In order to further verify that 20 samples are sufficient to run a reliable process capability analysis, the same measurements were analyzed when 150 samples were tested in the reactive near-field sub-region. Relevant process capability and probability plots are presented in Figures 4.5 and 4.6 and shown to yield similar Cpk values. Again, only two plots are included since they were representatives of the trend observed in all bands and technologies. With this in mind, we can rest assured that 20 samples provide reliable data.

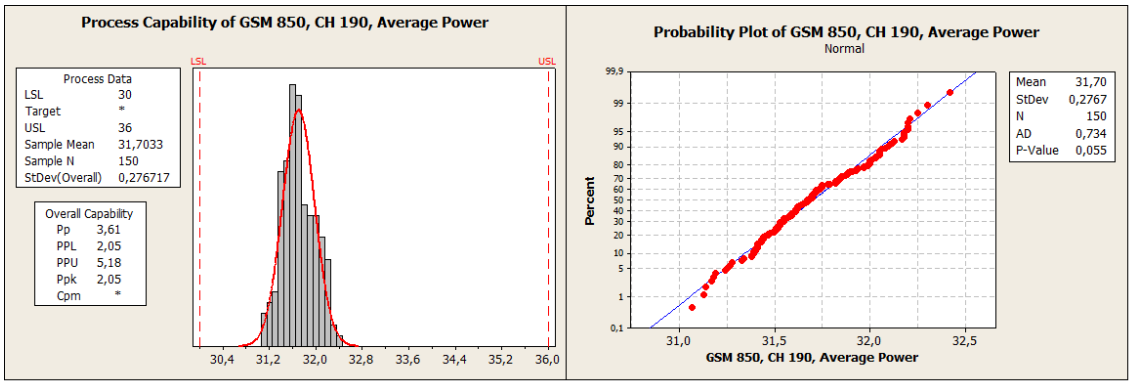

Figure 4.5: Process capability and Probability plot of output power in GSM 850.

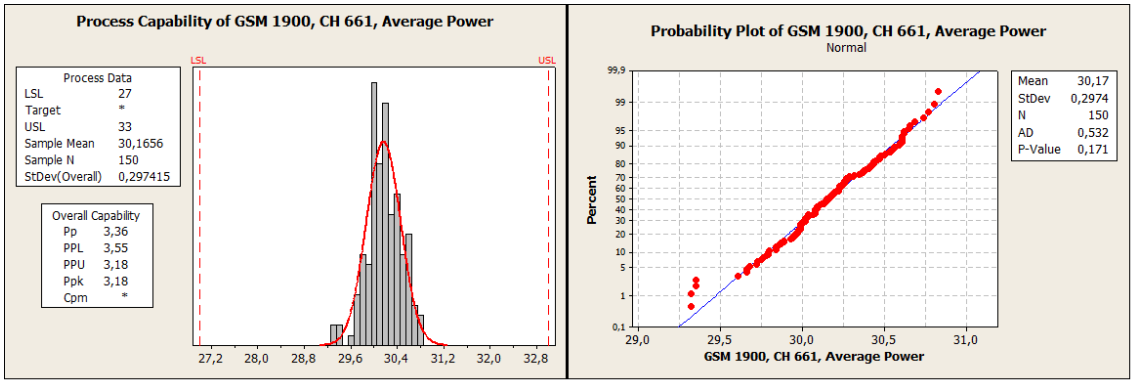

Figure 4.6: Process capability and Probability plot of output power in PCS 1900.

Figures 4.7 and 4.8 illustrate the process capability and probability plots of the reference sensitivity in GSM 850, and output power in PCS 1900, respectively.

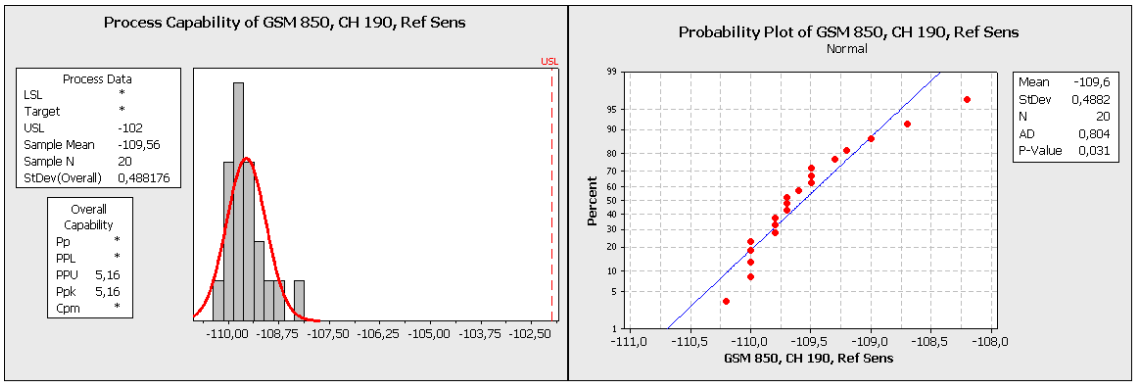

Figure 4.7: Process capability and Probability plot of reference sensitivity in GSM 850

Note that, as shown in Figure 4.7, only Cpk indices are calculated for parameters with one-sided specifications since a Cp index, as rendered by Equation 2.46, becomes meaningless. In effect, in such case no variation range in defined. Let us see how WCDMA technologies fare in their capability. Figure 4.9 shows the process capability and probability of the maximum output power in WCDMA, band II, and once again the capability of the phones to comply with the set specifications is verified.

Figures 4.10 and 4.11 show the process capability and probability plots of the maximum output power and reference sensitivity in WCDMA (band V), respectively; it is observed that the Cpk value in the output power, 1.21, falls short of the 1.5 margin set in Six Sigma process control. Notwithstanding the process being within the specification limits, the spread of its normal distribution is causing the low Cpk value and in particular, a sample is seen to be unacceptably near the upper specification limit. As it was pointed in Section 3.2, a convenient way to overcome this issue is by choosing another sweet spot. Following the same criteria described

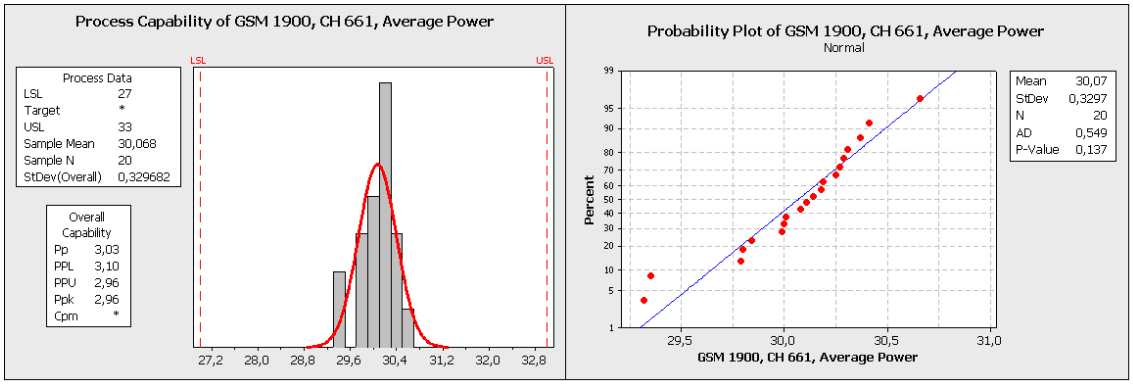

Figure 4.8: Process capability and Probability plot of output power in PCS 1900

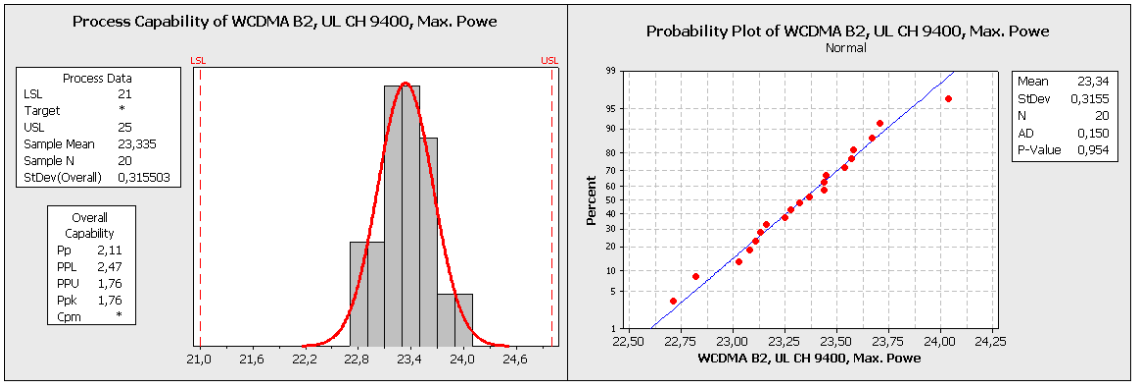

Figure 4.9: Process capability and Probability plot of output power in WCDMA II

therein, an alternative sweet spot was found where the spread of process distribution was reduced and the process capability improved accordingly. Figure 4.12 shows the same process capability and probability plots illustrated in Figure 4.10, but now the phones were positioned on a different sweet spot. The Cpk value of the reference sensitivity level in the same parameter was also increased from 1.66 to 2.42. The latter is illustrated by comparing Figures 4.11 and 4.13.

Finally, the process capability and probability plots of the maximum output power levels in LTE B4 and B17 are shown in Figures 4.14 and 4.15, as well as those of the throughput in LTE B4 and B17, as illustrated in Figures 4.16 and 4.17. Remember that in Section 4.1.3 it was said that the reference sensitivity level in LTE is measured by way of testing the throughput when the specified sensitivity levels are fixed. The throughput results from our measurements were free of bit errors and constant that no variation arose when all the samples were accounted for. Therefore, the software tool produced Cpk values of 999,99. This only means that the reference sensitivity level specified by 3GPP was indeed met in all cases, since the same result was obtained for all LTE bands.

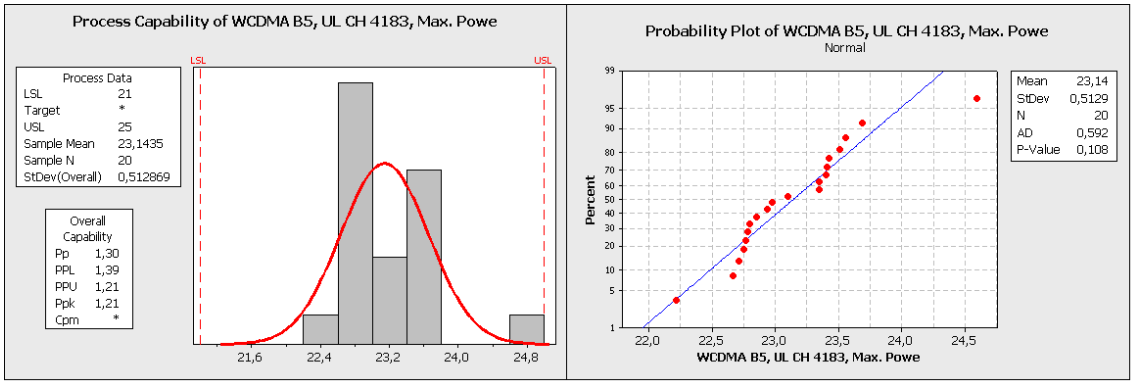

Figure 4.10: Process capability and Probability plot of output power in WCDMA V

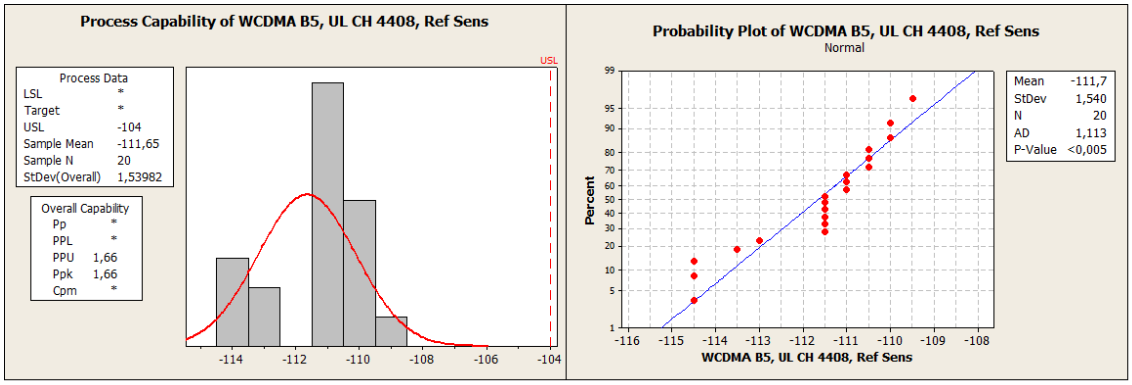

Figure 4.11: Process capability and Probability plot of reference sensitivity in WCDMA V

4.3.2 RF parametric evaluation and Cpk analysis when phone is at 6cm from antenna coupler (radiating near-field sub-region)

We have seen that the radiating near-field sub-region is demarcated by a radius $R_2 = 5\lambda$. Once more as it was done in the previous section, a check across the test frequencies sets a particular frequency band as the limiting radius. In this case, however, it is the lowest frequency band the dominating factor and provides the smallest radius for the reactive near-field sub-region, $R_1 = 0.16\lambda$ Indeed, by selecting the lowest frequency (709MHz) under test, LTE B17 low channel, we obtain a radius $R_1 = 6.68cm$. This posed a challenge to our study because the 6-cm gap between the antenna coupler and the phone does not situate the latter in the radiating near-field. When different sweet spots were searched at various distances from the antenna coupler, it was observed that 6cm provided an acceptable level of coupling loss and a flat response across the frequency bands of interest. Larger distances were investigated but in fact, the dimensions of the RF shield box restrained the maximum allowable gap.

When the phone was placed at about 10cm from the coupler, the top case of the

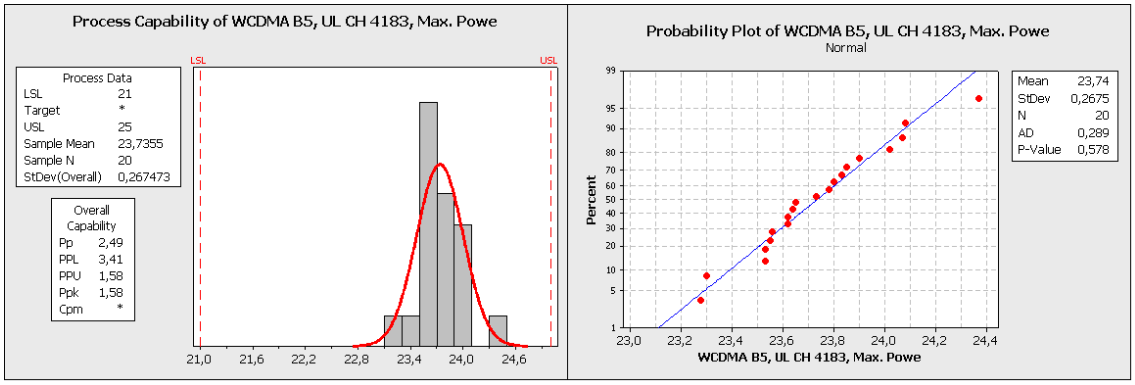

Figure 4.12: Process capability and Probability plot of output power in WCDMA V, where measurements were made on alternative sweet spot.

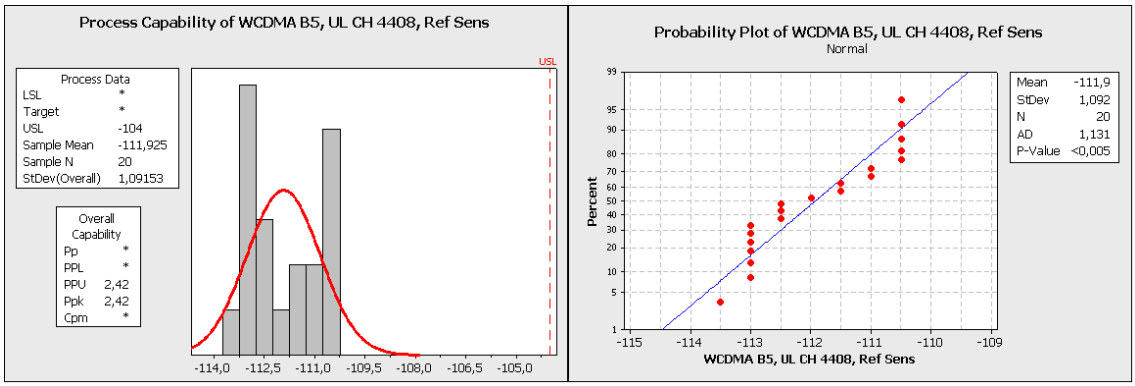

Figure 4.13: Process capability and Probability plot of reference sensitivity in WCDMA V, where measurements were made on alternative sweet spot.

RF shield box was nearly touching the phone when it was closed. Consequently, in order to test this troublesome frequency band with the phone placed at 11cm from the antenna coupler (this distance proved to fulfill the selection criteria of the sweet spot), the plate where the antenna coupler was embedded in the RF shield box was removed and the antenna coupler was placed at the bottom of the box. This kept the phones away from the top case when closed and yet, it only served its purpose for the particular frequency band and for the sake of obtaining reliable measurements in the radiating near-field sub-region under test because the plate was fundamental to hold the phones in the same sweet spot. Figure 4.18 shows the process capability and probability plots of the maximum output power at the lowest frequency tested, 709MHz, when the phone is 11cm from the antenna coupler. It is observed that when the phones are tested in the radiating near-field sub-region at this limiting frequency, the resulting process is capable of meeting the specifications. Similar graphical representations as the ones shown above were obtained for the remaining maximum output power and reference sensitivity levels in GSM, WCDMA and LTE technologies. Therefore they will be omitted and instead, we present a summary

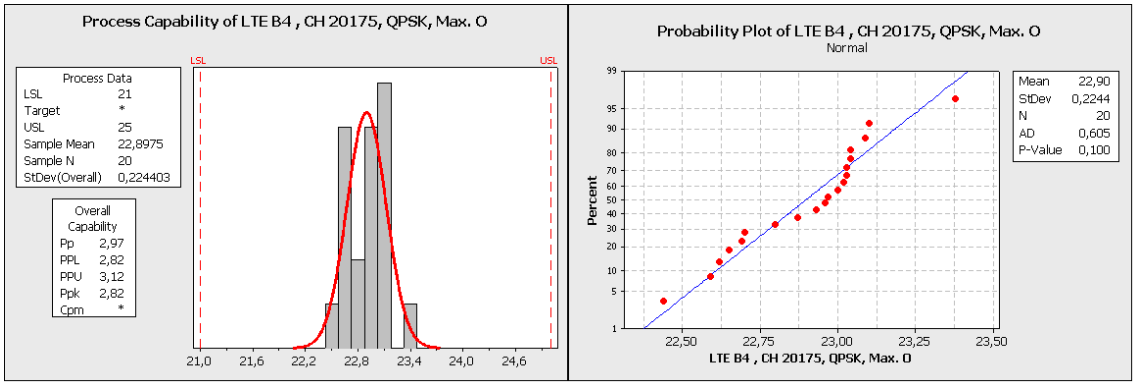

Figure 4.14: Process capability and Probability plot of output power in LTE B4.

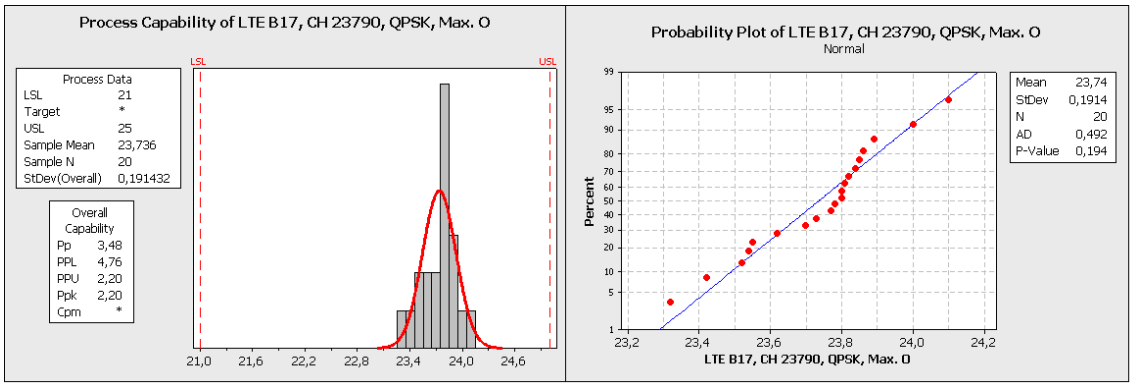

Figure 4.15: Process capability and Probability plot of output power in LTE B17.

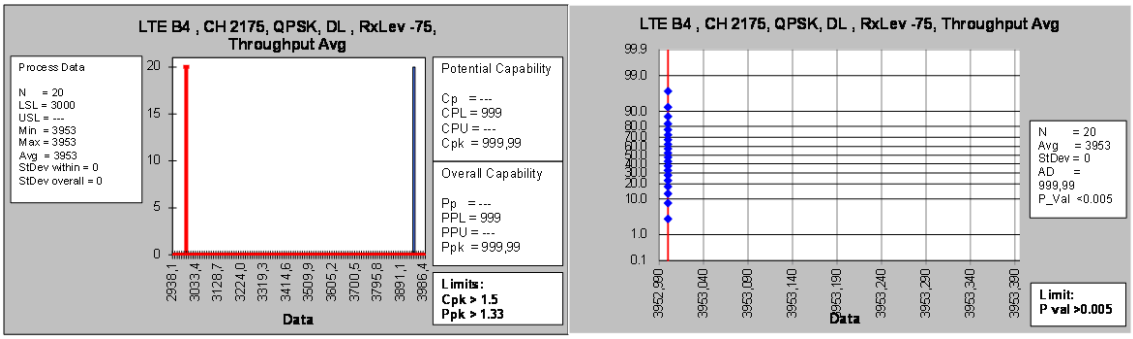

Figure 4.16: Process capability and Probability plot of throughput in LTE B4.

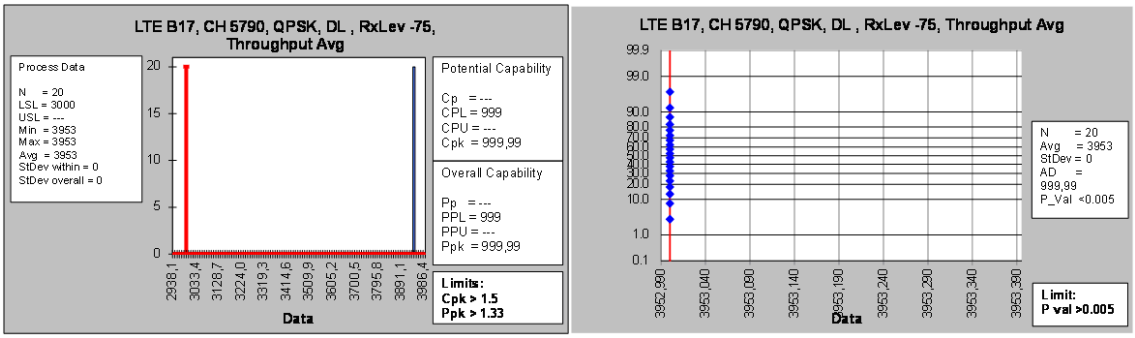

Figure 4.17: Process capability and Probability plot of throughput in LTE B17.

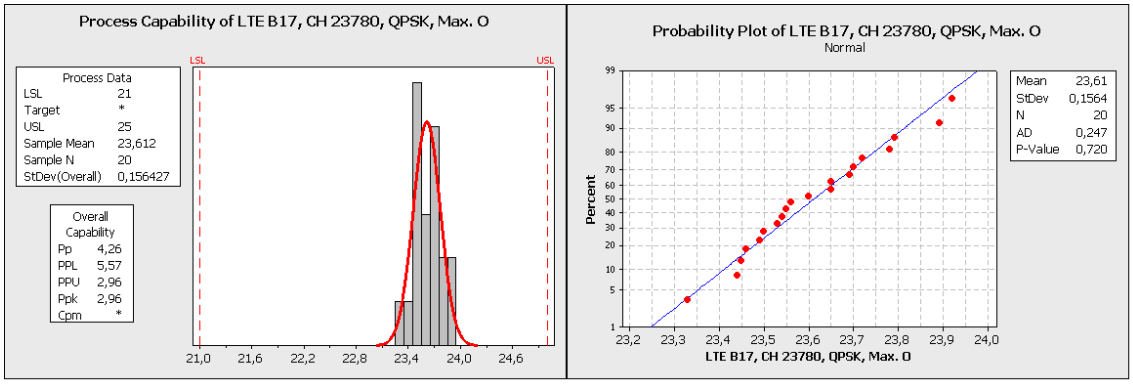

Figure 4.18: Process capability and Probability plot of Maximum output power in LTE B17, low channel.

of all the Cpk results in all parameters presented in the foregoing Sections, for both the reactive and radiating near-field regions. Table 4.7 summarizes the process capability indices, Cpk, of the measurement results presented previously.

Table 4.7: Summary of Process Capability indices, Cpk, yielded by RF radiated measurements conducted in the reactive and radiating near-field sub-regions.

	Reactive near-field			***Radiating near-field***		
Measurement Parameters	***Low CH***	***Middle CH***	***High CH***	***Low CH***	***Middle CH***	***High CH***
GSM 850						
TX Power	2.53	2.03	2.14	1.94	1.82	1.69
RMS Phase Error	68.36	52.15	40.35	76.17	72	96.4
Peak Phase Error	101.5	83.2	68.9	88.72	78.68	103.34
Frequency Error [1]		5.9			9.25	
BER Sensitivity Search	6.16	5.16	3.7	10.34	2.82	5.31
PCS 1900						
TX Power	2.47	2.96	2.67	4.28	4.12	2.8
RMS Phase Error	15.1	22	25.93	30.43	31.27	29.35
Peak Phase Error	25.8	35.47	34.27	42.8	41.98	40.71
Frequency Error [1]		15.9			10.79	
BER Sensitivity	3.92	4.5	4.3	5.51	6.42	6.96
WCDMA II						
Max. Output Power	1.83	1.76	2.32	4.61	4.27	3.02
Error Vector Magnitude	14.84	16.3	11.28	11.6	11.41	8.77

continued on next page

continued from previous page

	Reactive near-field			***Radiating near-field***		
Measurement Parameters	***Low CH***	***Middle CH***	***High CH***	***Low CH***	***Middle CH***	***High CH***
Frequency Error	41.1	189.5	48.9	70.4	330.31	72.32
Ref. Sensitivity	2.5	2.36	3.26	2.84	4.89	3.09
WCDMA V						
Max. Output Power [2]	1.68	1.58	1.64	2.48	2.84	2.13
Error Vector Magnitude	20.9	26	7.3	24	20.6	16.55
Frequency Error	46.27	412.8	46.5	52.03	287.76	78.06
Ref. Sensitivity [2]	3.26	2.42	1.69	1.8	1.59	2.13
LTE B4						
Max. Output Power	2.42	2.82	2.75	3.61	4.58	4.17
Error Vector Magnitude	37.5	33.6	35.3	4.85	5.17	14
Carrier Leakage	1.1	1.03	0.98	0.76	0.62	0.62
Frequency Error	170.4	65.5	74.7	6.9	7.16	58.42
ACLR E-UTRA	8.28	6.54	6.17	10.44	4.91	8
Data throughput	999.99	999.99	999.99	999.99	999.99	999.99
LTE B17				[3]	[3]	[3]
Max. Output Power	1.88	2.2	2.08	2.96	2.85	3.1
Error Vector Magnitude	5.13	47.8	76.9	55.53	36.68	45
Carrier Leakage	0.68	0.7	1.07	1.13	1.07	1.1
Frequency Error	3.16	63.37	62.23	74.93	52.48	60.5
ACLR E-UTRA	5.6	6.67	12.5	4.69	3.98	9.94
Data throughput	999.99	999.99	999.99	999.99	999.99	999.99

The process capability indices in Table 4.7 support the claim that RF radiated measurements as described in this thesis can indeed be conducted by placing the phones in the reactive or radiating near-field regions. It is observed that the process is capable of meeting the set specifications in both near-field sub-regions.

An interesting case occurs with the carrier leakage parameter in LTE, where the Cpk values are well below the 1.5 margin. Figure 4.19 illustrates the lowest Cpk value obtained when measuring the carrier leakage. It appeared in the middle and high channels of LTE B4. Although the process exhibits a fair normal distribution, it is evidently its wide spread the root cause for the low Cpk value. This is not a problem because this parameter is a one-sided specification process for which greater carrier

[1] Due to some error while configuring the settings of the software running the test sequence, the frequency error was only measured in the middle channels in 2G

[2] These Cpk values were obtained from alternative sweet spots

[3] Measurements made with phones and antenna coupler distanced by 11cm

leakage ratios are indicative of even better conformance to the -25dBc specification.

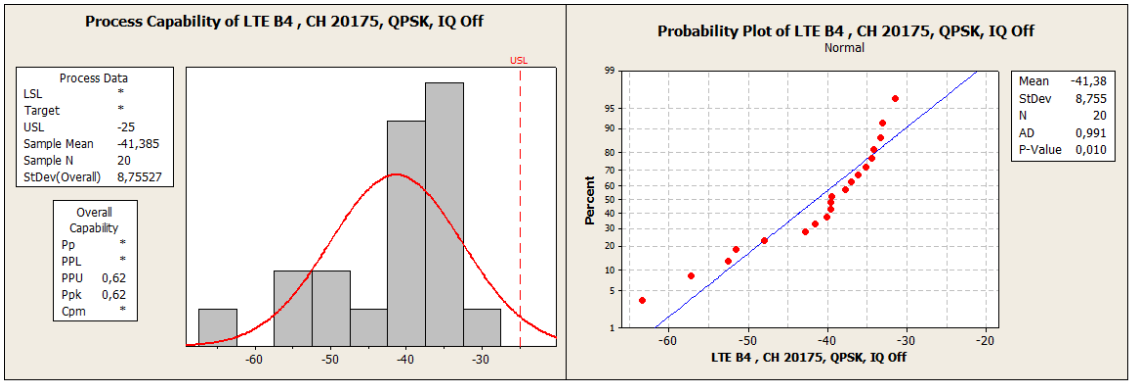

Figure 4.19: Process capability and Probability plot of carrier leakage in LTE B4.

By and large, slightly better Cpk values (in most frequency bands and particularly when it involved sensitivity measurements) would seem to favor the selection of the radiating sub-region as the location to place the phones but in any case, the process capability rendered by conducting the measurements in the reactive sub-region was also demonstrated to be capable of fulfilling the same specifications. Finally, it has been indicated that a fundamental condition to obtain accurate and reliable results is to have a good repeatability during the entire measurement process, by ensuring that the phones are fixed in exactly the same position. A valuable aid in achieving this is by using a jig [5] where each and every phone can be held in exactly the same sweet spot every time a measurement is run. Making the measurements in the reactive region may facilitate the construction of such a jig (as it was our case) and make it more affordable if the material used for the fabrication may be costly due to a harder and thus sturdier structure that can guarantee a good durability over many measurements. Moreover, a significant challenge may arise when the measurements are made in the radiating near-field for low frequency bands due to the reduced dimensions of RF shield boxes.

4.3.3 Uncertainties in radiated measurements

The last two sections have shown the process capability results calculated from our measurements in both near-field sub-regions. The Cpk values have validated the compliance of the RF performance of the phones to the 3GPP specifications. In addition to the process capability analysis, a comparison was made between our radiated RF measurement results and the results obtained on the same RF parameters performed in a conducted manner, and also some of the parameters from measurements made in an OTA environment. Due to confidentiality issues, a

[5] A jig was designed and made by a colleague for making the measurements in the reactive near-field region.

disclosure of those additional results is not possible. It suffices for our verification purposes, that our results were found to be in good agreement with those made in both conducted and OTA setups. However, some small differences arose in certain parameters. For example, readings of maximum output power levels or reference sensitivity values varied in some cases a couple of dB. This may be owing to the uncertainties proper to each testing environment. This section provides a rough assessment of the possible uncertainties found in my measurement setup.

In any measurement system, it is never possible to measure the actual value since a level of uncertainty or error will always be present. The accuracy of a measurement, therefore, is defined in terms of the uncertainty boundaries within which it is estimated that the actual value lies. The idea of uncertainty in a measurement underlies the fact that the measured value is one of an infinite number of possible values spread about that value that happened to be measured. The method used in this thesis for assessing the uncertainty boundaries corresponds to the one described in [42]. This method is referred to as the *combined standard uncertainty*. The principle of this technique is to calculate the measurement uncertainty by combining the standard uncertainties for each individual contribution. This is done by applying the Root of the Sum of the Squares (RSS) method where it is assumed that all contributions are independent of each other. The overall combined standard uncertainty is then multiplied by a constant k_{xx} to provide the uncertainty limits, known as *expanded uncertainty*, at a confidence level of $xx\%$ [42, p. 20]. The confidence level is defined therein as the probability of the accumulated error of a measurement to be within the stated range of uncertainty.

Two types of uncertainties are identified in [42]. A type A comprising uncertainties that are evaluated by statistical methods, and type B uncertainties evaluated by other means. Both types have probability distributions, and the uncertainty elements derived from either type are quantified by standard deviations. Type B uncertainties remain constant and can be found in the form of mismatch, losses in cables, non-linearities in instruments, among others [42, p. 24, 25]. The document also distinguishes three types of uncertainty distributions in RF measurements: "U" distribution, rectangular distribution, and normal (Gaussian) distribution. Mismatch (media with different characteristic impedances) have the "U" distribution, while systematic uncertainties are said to have a rectangular distribution. The standard uncertainties for such distributions are to be calculated by a multiplying factor. In case of mismatch uncertainties, [42, p. 29] states that the value of the uncertainty contribution is less likely to be near zero, and rather it will be close to the limits. Thus, if the uncertainty limits are $\pm a$, the standard uncertainty is given by:

$$\frac{a}{\sqrt{2}}. \tag{4.1}$$

Systematic uncertainties, on the other hand, are generally assumed to have a rectangular distribution [42, p. 29] and as such, the uncertainty value is said to lie anywhere between the limits with the same likelihood. If the limits are again $\pm a$, the standard uncertainty is given by:

$$\frac{a}{\sqrt{3}}. \tag{4.2}$$

When the distribution used in the model is unknown, it is recommended to assume a rectangular distribution as the default choice [42]. The combined standard uncertainty is obtained by the root of the sum of the squared individual standard uncertainties, and given by:

$$u_C = \sqrt{u_{j1}^2 + u_{j2}^2 + \cdots + u_{j(n-1)}^2 + u_{jn}^2}, \tag{4.3}$$

which is predicated on the assumption that the individual contributions combine by addition, and are expressed in the same units [42]. The former condition implies that each standard uncertainty is a linear term, while the latter demands the use of some conversion factors when we are dealing with different units. For instance when converting a standard uncertainty from dB units to voltage percentage % units, a multiplying conversion factor of 11.5 must be used [42, p. 30]. This conversion factor is used below when calculating the uncertainty due to an impedance mismatch. After deriving the combined standard uncertainty, the expanded uncertainty for a 95% confidence level is then computed by using the Student's t-distribution [6] factor of 1.96. This factor is applied to an infinite number of samples, but is equally valid to even a single sample as long as all the magnitudes of individual uncertainties and their distributions are known [42]. An approximate calculation of the combined standard uncertainty in the radiated measurements presented in this thesis is described next. It is intended to include the most relevant contributors to uncertainty, but it does not represent an exhaustive analysis. The calculated value, however, should provide an approximate magnitude of uncertainty to be expected in the measurements in a worst-case scenario where the maximum level of individual uncertainties occur simultaneously. All the individual uncertainty contributors encountered are type B. First, we begin by computing the standard uncertainty due to a mismatch. We consider only the mismatch at the RF port of the radio communication tester, which is derived from a VSWR of 1.2 provided by the manufacturer. Having the VSWR, we can obtain the voltage reflection coefficient from Equation 2.40, which is given as $\Gamma = 0.09$. The standard uncertainty due to this mismatch is calculated

[6] Student's t distribution is a set of continuous probability distributions that arises when estimating the mean of a normally distributed population in cases where the sample size is small and the standard deviation unknown [Wikipedia].

by [42, p. 34]

$$u_{j(mismatch)} = \frac{|\Gamma| \times |S_{21}| \times |S_{12}| \times 100\%}{\sqrt{2} \times 11.5}[dB],$$

where only the reflection coefficient at the generator is considered, $|S_{21}| = |S_{12}| = 1$, and the factor 11.5 is used to convert units from voltage percentage to dB. The mismatch standard uncertainty is calculated to be 0.55dB. Note that the $\sqrt{2}$ factor denotes a "U" distribution. A standard uncertainty due to the attenuation of the coaxial cable connecting the radio communication tester and the RF shield box is calculated next. The length of the high-performance cable used is roughly 1.5m. Figure **??** showed the attenuation per meter with respect to frequency of the coaxial cable used in our measurements. By assuming a pessimistic value of 0.5dB/m (which occurs at frequencies a little above 2GHz), and as noted a length of 1.5m, the total attenuation for our cable is given as 0.75dB, and the corresponding standard uncertainty (from Equation 4.2) is 0.43dB. The manufacturer of the radio communication tester also provides an output level uncertainty of 0.6dB, and its standard uncertainty, once again derived from Equation 4.2 since no distribution is given, is found to be 0.34dB. The manufacturer of the RF shield box (including the antenna coupler) provided an uncertainty level of 2.5dB. Equation 4.2 gives the standard uncertainty as 1.44dB. The combined standard uncertainty of the above contributions, as yielded by Equation 4.3, is calculated as 1.64dB. The expanded uncertainty is $\pm$ 1.64dB $\times$ 1.96 = $\pm$ 3.21dB at a 95% of confidence level.

5. CONCLUSIONS

This thesis has presented a study on radiated RF measurements. The measurements served to evaluate the performance of the most relevant RF parameters on 4G smart phones and were part of a project carried out in Nokia corporation. A measurement system consisting mainly of a radio communication tester, an RF shield box and an antenna coupler was set up and used for the tests. Due to the dimensions of the RF shield box, measurements were conducted in the near-field region. Measurements were performed in both the reactive and the radiating near-field sub-regions, and in both cases the results obtained complied with the specifications set by 3GPP standards. A threefold verification of the results was conducted mainly by a process capability analysis, and also by comparing my results with those obtained in the company from conducted RF measurements and OTA test results. Over the course of the project, additional analyses were found worthy of further study as is proposed at the end of the conclusions.

The accuracy and reliability of my results presupposed those of the measurement system. This comprised on the one hand, a robust measurement setup where all sources of error were identified and duly minimized if not eliminated, and also the selection of an appropriate position where each and every phone could be tested. Proper to the particular setup where I conducted the measurements, a substantial error to the accuracy of the measurements was caused by deleterious reflections inside the RF shield box. This was due to the lack of any RF absorber material at the bottom of the RF shield box, and was readily circumvented by adding a layer of carbonyl iron loaded urethane rubber at the bottom of the RF shield box. My measurements suggested that a single layer was enough to mitigate the reflections and, as opposed to using two such layers, one layer allowed me to obtain slightly better process capability results. In addition, paramount to obtaining accurate results was the selection of an appropriate spot where the phones were tested. Based on S21 measurements described in Chapter 3, I set three criteria to guide my search of such 'sweet spot': the attenuation response would need to be as flat and low as possible across the frequency bands to be tested, and the selection of preferably a unique sweet spot where good results could be obtained across all frequency bands. The last criterion proved to be very difficult to fulfill, and eventually was relaxed to two sweet spots. Once a suitable spot was found, it was necessary to ensure good

repeatability of the measurements by holding each phone at exactly the same position. A custom-made jig facilitated this in the reactive sub-region, and a Styrofoam structure in the radiating sub-region.

In order to establish the validity of my measurements, a statistical process capability has been performed. A Cpk of 1.5, as recommended by the Six Sigma quality control standard for different industry sectors, has been chosen as the benchmark to evaluate the conformity of my measurement results to the specifications prescribed by 3GPP. The Cpk results presented in Chapter 4 validate the compliance of the RF parameters evaluated on the phones, both in the reactive and radiating near-field sub-regions. In general, slightly better Cpk values were obtained from the radiating sub-region, especially for sensitivity measurements. However, care should be taken to ensure that the distance of the location of the phones in the radiating sub-region is not too large that exceeds the dimensions of the RF shield box. This occurs if the testing frequency is not high enough. For example in our measurements, LTE B17 set the testing height at 11cm above the antenna coupler. It may not be feasible then to test lower frequencies (for example, LTE 450MHz) in this particular sub-region.

I have also indicated a further step to validate my results. Although a disclosure of the measurement results obtained from conducted RF and OTA testing environments is not possible, it suffices to state that my measurement results were in good agreement with those obtained from the latter. Small differences appeared in some cases (for instance, a couple of dB in power measurements), and that may be due to the uncertainties proper to each testing system. In case of my test system, an approximate assessment of the level of uncertainty was derived and quantified.

Further research can be derived from the present thesis. For instance, at the very outset of our study it was pondered whether to perform a full electromagnetic simulation analysis on the whole measurement setup. Although discarded because of a dearth of resources and time, such computational study would shed valuable light on the electromagnetic analysis and be subsequently used in finding a sweet spot by analyzing the behavior of EM fields inside the RF shield box. Also, further investigations can be devoted to a rigorous analysis and quantification of uncertainties in radiated measurements made in the setup described herein. Finally, an interesting analysis could be performed to observe the interaction and effects a multiple-antenna handset has on the measurements in question. A great deal of 4G smart phones incorporate main and diversity antennas whose performance (both in a stand-alone and a diversity mode) will invariably affect the coupling with the antenna coupler inside the RF shield box, and will influence the performance of the RF parameters.

REFERENCES

[1] Prasad, S. & Beckman, C. Comparison of Four Different Methods to Estimate the Radiated Power from Mobile Phones. Conference on Antennas and Propagation. 2010, pp. 425-428.

[2] Pozar, D. M. Microwave Engineering. Third ed. United States 2005. John Wiley & Sons, Inc. 700 p.

[3] Ramo, S., Whinnery, J. R. & Van Duzer, T. Fields and Waves in Communication Electronics, United States 1965. John Wiley & Sons, Inc. 754 p.

[4] Cheng, D. K. Fundamentals of Engineering Electromagnetics, United States 1993. Addison-Wesley. 488 p.

[5] Guru, B. S., Hiziroglu, H. R. Electromagnetic Field Theory Fundamentals, United States 2004. Cambridge University Press. 680 p.

[6] Stutzman, W. L. & Thiele G.A. Antenna Theory and Design, United States 2013. John Wiley & Sons, Inc. 822 p.

[7] Fusco, V. F. Foundations of Antenna Theory and Techniques, England 2005. Pearson Education Limited. 230 p.

[8] Schelkunoff, S. A. & Friis H. T. Antenna Theory and Practice, United States 1952. John Wiley & Sons, Inc. 639 p.

[9] Balanis, C. A. Antenna Theory. Third ed. United States 2005. John Wiley & Sons, Inc. 1099 p.

[10] Blake, L. V. & Long, M.W. Antennas: Fundamentals, Design, Measurement. Third ed. United States 2009. Scitech Publishing, Inc. 503 p.

[11] Richards, M. A., Scheer, J. A. & Holm, W. A. Principles of Modern Radar, United States 2010 . Scitech Publishing, Inc. 924 p.

[12] DeVor, R. E., Chang, T. & Sutherland, J.W. Statistical Quality Design and Control, Contemporary Concepts and Methods. First ed. United States 1992. Macmillan Publishing Company. 809 p.

[13] Ryan, T. P. Modern Engineering Statistics. First ed. United States 2007. John Wiley & Sons, Inc. 586 p.

[14] Dekking, F.M., Kraaikamp, C., Lopuhaä, H. P., Meester, L. E. A Modern Introduction to Probability and Statistics. First ed. United States 2005. Springer-Verlag London Limited. 504 p.

[15] http://www.minitab.com/en-us/. Accessed on 06 April 2014.

[16] Shina, S. G. Six Sigma for Electronics Design and Manufacturing. First ed. United States 2002. McGraw-Hill. 363 p.

[17] Stapenhurst, T. Mastering Statistical Process Control. First ed. United States 2005. Elsevier. 456 p.

[18] Mini Paper, Process Capability Indices by R. H. Mitchell. http://asq.org/statistics/2010/09/quality-tools/process-capability-indices.pdf. Accessed on 10 December 2013.

[19] Zhang, Z. Antenna Design for Mobile Devices. First ed. Singapore 2011. John Wiley & Sons (Asia) Ltd. 304 p.

[20] Hemming, L. H. Architectural Electromagnetic Shielding Handbook: A Design and Specification Guide. First ed. United States 1992. IEEE Publications. 240 p.

[21] Shastry, S.V.K., Nagesh, S.K. & Rao, M.N. Dipole Excitation of RF Shielded Chamber. International Conference on Electromagnetic Interference and Compatibility. 1995, pp. 230-236.

[22] Shastry, S.V.K., Nagesh, S.K. & Binu, D. Reflectivity Level of RF Shielded Anechoic Chamber. IEEE International Symposium on Electromagnetic Compatibility. 1995, pp. 578-583.

[23] Stallings, D. C. An Approximate Theory of RF Shielded Enclosures . IEEE International Symposium on Electromagnetic Compatibility. 2012, pp. 629-634.

[24] RF Couplers for Mobile Phone Testing. White paper. http://www.willtek.com/mediadb/global/download/literature/white_papers/Willtek_RFcoupler_wp656_0404_en.pdf. Accessed on 14 September 2013.

[25] Andersson, M., Orlenius, C., & Kildal, P. Three Fast Ways of Measuring Receiver Sensitivity in a Reverberation Chamber. International Workshop on Antenna Technology: Small Antennas and Novel Metamaterials. 2008, pp. 51-54.

[26] Volakis, J. Antenna Engineering Handbook. Fourth ed. United States 2007. McGraw-Hill. 1800 p.

[27] Scott, A. W. & Frobenius, R. RF Measurements for Cellular Phones and Wireless Data Systems. First ed. United States 2007. John Wiley & Sons, Inc. 528 p.

[28] Complete Coaxial Cable Catalog & Handbook, 15th ed., Times Microwave Systems. http://www.timesmicrowave.com/products/tl14/downloads/tl15_catalog.pdf. Accessed on 10 October 2013.

[29] Factors to Consider for High Performance Coaxial Cables. Tutorial. http://www.highfrequencyelectronics.com/Archives/Aug11/HFE0811_Tutorial.pdf. Accessed on 10 October 2013.

[30] Notes on the Selection Criteria for Coaxial Cables. Tutorial. http://www.highfrequencyelectronics.com/Archives/Sep10/HFE0910_tutorial.pdf. Accessed on 10 October 2013.

[31] Wolff, E. A. & Kaul, R. Microwave Engineering and Systems Applications, United States 1988. John Wiley & Sons, Inc. 641 p.

[32] Clarricoats, P. J. B. & Barlow, H. M. Microwave Ferrites, London 1961. Chapman & Hall, Ltd. 260 p.

[33] Using Ferrites for Interference Suppresion. http://www.elmac.co.uk/pdfs/ferrite.pdf. Accessed on 12 October 2013.

[34] Antenna Standards Committee of the IEEE Antennas and Propagation Society. IEEE Standard Definitions of Terms for Antennas . IEEE Antennas and Propagation Society. 2013, pp. 1-32.

[35] http://www.3gpp.org/About-3GPP. Accessed on 30 October 2013.

[36] Digital cellular telecommunications system (Phase 2+); Mobile Station (MS) conformance specification; Part 1: Conformance specification (3GPP TS 51.010-1 version 10.2.0 Release 10) . http://www.etsi.org/deliver/etsi_ts/151000_151099/15101001/10.02.00_60/ts_15101001v100200p.pdf. Accessed on 30 October 2013.

[37] Digital cellular telecommunications system (Phase 2+);Radio Transmission and Reception (3GPP TS 05.05 version 8.18.0 Release 1999). http://www.etsi.org/deliver/etsi_ts/100900_100999/100910/08.18.00_60/ts_100910v081800p.pdf. Accessed on 30 October 2013.

[38] Universal Mobile Telecommunications System (UMTS); User Equipment (UE) conformance specification; Radio transmission and reception (FDD); Part 1: Conformance specification (3GPP TS 34.121-1 version 10.5.0 Release 10). http://www.etsi.org/deliver/etsi_ts/134100_134199/13412101/10.05.00_60/ts_13412101v100500p.pdf. Accessed on 30 October 2013.

[39] Geßner, C. Long Term Evolution, A concise Introduction to LTE and Its Measurement Requirement, Germany 2011. Rohde & Schwarz GmbH & Co. 219 p.

[40] LTE; Evolved Universal Terrestrial Radio Access (E-UTRA); User Equipment (UE) conformance specification; Radio transmission and reception; Part 1: Conformance testing (3GPP TS 36.521-1 version 11.1.0 Release 11) . http://www.etsi.org/deliver/etsi_ts/136500_136599/13652101/11.01.00_60/ts_13652101v110100p.pdf. Accessed on 30 October 2013.

[41] R&S®CMW-Z11 and R&S®CMU200 Determining the Path Loss, Application Sheet. http://www.rohde-schwarz.ca/file/DST200_CMU_Path_Loss_Measurement.pdf. Accessed on 15 November 2013.

[42] Electromagnetic compatibility and Radio spectrum Matters (ERM); Improvement of radiated methods of measurement (using test sites) and evaluation of the corresponding measurement uncertainties; Part 1: Uncertainties in the measurement of mobile radio equipment characteristics; Sub-part 1: Introduction. http://www.etsi.org/deliver/etsi_etr/200_299/2730101/01_60/etr_2730101e01p.pdf. Accessed on 2 January 2014.